

The Formation and Evolution of Protostellar Disks; 3D AMR Hydro-Simulations of Collapsing, Rotating Bonnor-Ebert-Spheres

Robi Banerjee¹, Ralph E. Pudritz and Lindsay Holmes

¹*Sharcnet Postdoctoral Fellow*

Department of Physics and Astronomy, McMaster University, Hamilton, Ontario L8S 4M1, Canada

14 November 2018

ABSTRACT

We present a detailed study of the collapse of molecular cloud cores using high resolution 3D adaptive mesh refinement (AMR) numerical simulations. In this first in a series of investigations our initial conditions consists of spherical molecular core obeying the hydrostatic Bonnor-Ebert-Profile with varying degrees of initial rotation. Our simulations cover both the formation of massive disks in which massive stars form as well as low mass disks. We use a customized version of the FLASH code whose AMR technique allows us to follow the formation of a protostellar disk and protostellar core(s) through more than ten orders in density increase while continuously resolving the local Jeans length (i.e. obeying the Truelove criterion, Truelove et al. (1997)). Our numerical simulations also incorporate the energy loss due to molecular line emission in order to obtain a more realistic picture of protostellar core and disk formation. Our initial states model system of mass $168 M_{\odot}$ and $2.1 M_{\odot}$ that will form high and low mass stars, respectively. We follow many features such as the development complex shock structures, and the possible fragmentation of the disk. We find that slowly rotating cores ($\Omega t_{\text{ff}} = 0.1$) produce disks in which a strong bar develops but which does not fragment. Faster initial rotation rates ($\Omega t_{\text{ff}} = 0.2$) result in the formation of a ring which may fragment into two star-forming cores. The size of the rings found in our simulated disks agree with the observations of similar systems.

Key words: accretion, accretion discs, hydrodynamics, ISM: clouds, evolution, methods: numerical

1 INTRODUCTION

The formation of protostars and their surrounding disks from collapsing, dense, molecular cores within molecular clouds is still an actively debated topic. Early pioneering works by Bodenheimer & Sweigart (1968), Larson (1969), and Penston (1969) addressed this problem using numerical simulations for various initial conditions. Bodenheimer & Sweigart studied collapses of isothermal spherical symmetric gas clouds which are initially out of equilibrium. They pointed out that the solutions depend only very weakly on the choice of the initial density profile (homogeneous or Chandrasekhar-type). Larson (1969) and Penston (1969) included the effect of energy dissipation by radiation in their 1D simulations and found that cooling during the initial collapse phase is efficient enough to keep the gas at its initial temperature. Although both studies start with different initial conditions (Larson used a homogeneous density distribution whereas Penston used a Bonnor-Ebert-Profile) they obtained similar results during the isothermal collapse. Starting with a highly unstable, initial singular

isothermal sphere Shu (1977) obtained a different evolution scenario: a self-similar inside-out collapse and claimed that the former solutions are physically artificial. Hunter (1977) in his study of unstable isothermal spheres pointed out that both investigations address the same problem but refer to two different stages of the isothermal collapse. The Larson-Penston studies investigate the collapse of molecular clouds prior to the formation of protostellar core whereas Shu's study apply to the accretion phase of a non-rotating cloud with a central protostar.

In reality, molecular cores have some initial angular momentum so that most of the collapsing material ends up in a rotating accretion disk (due to their non-vanishing initial angular momentum). This significantly alters the dynamics of the protostellar core's evolution. More recently, this issue was addressed with the help of 2D and 3D numerical simulations by several groups (for a review see Bodenheimer et al. 2000). For instance Burkert & Bodenheimer (1993) studied the fragmentation of a rotating sphere of uniform density with a $m = 2$ perturbation on a fixed nested grid. Their simulations showed that a bar formed which then fragmented into

two low mass binaries and several lighter secondary fragments. Truelove et al. (1998) used a 3D AMR technique that resolves the local Jeans length throughout the simulation to reinvestigate the fragmentation problem. These authors found that a bar like structure collapses instead to a single filament without further fragmentation. These differences can be shown to depend upon the ability to resolve the local Jeans length during the collapse (e.g. review Bodenheimer et al. 2000). An equivalent requirement for SPH simulations was found by Bate & Burkert (1997) who showed that the minimal resolvable mass must be smaller than the Jeans mass to avoid numerical fragmentation. But these authors also noted that the inclusion of artificial viscosity and heating, which increases the Jeans length and slows the collapse, lead to physical fragmentation of bars which is predicted in the work of Inutsuka & Miyama (1992). Clouds with an initial Gaussian density profile were studied by Boss (1993) who concluded that the most sensitive parameter for clouds to fragment is α , the ratio of the thermal to gravitational energy.

Matsumoto & Hanawa (2003) did an extensive parameter study of rotating Bonnor-Ebert-Spheres with different rotation profiles and rotation speeds. Their investigations are based on a three dimensional nested grid technique which resolves the local Jeans length and the use of two different equation of states depending on the central density (an isothermal EOS in the low density regime and a barotropic EOS in the high density regime). They showed that the final structure of the collapsed cloud (bar, ring, or binary system) depend sensitively on the parameter $t_{\text{ff}} \Omega$, where t_{ff} and Ω are the initial free fall time and the angular velocity, respectively.

Another important physical process that alters the dynamics of the core formation and disk evolution is the cooling process during the collapsing phase. An often used simplification to account for the decreasing efficiency of the cooling mechanism is the previously mentioned sudden switch of the EOS, depending on the local density. We do not follow this approach but rather include the loss of energy due to molecular line emission by collisional excitations. In this work we show that the effective equation is a complex function of time, density, and space which influences the structure of the protoplanetary disk and its possible fragmentation.

The study of Bonnor-Ebert-Spheres as initial states for star formation are of particular interest because they resemble marginal stable molecular cores in pressure equilibrium and have flat topped rather than singular density profiles. Observed evidence for Bonnor-Ebert-type cores are found in a variety of molecular clouds (e.g. Racca et al. 2002; Harvey et al. 2001; Alves et al. 2001) and in numerical simulations of star cluster formation in molecular clouds (Tilley & Pudritz 2004). The observation of massive disks undergoing high mass star formation (Chini et al. 2004) suggests that a similar scenario pertains to massive star formation (e.g. Yorke & Sonnhalter 2002).

In this paper we investigate low and high mass star formation from rotating molecular cores through AMR simulations. This paper is organized as follows: in Sec. 2 we explain our numerical scheme including the cooling procedure, and summarize the properties of the static Bonnor-Ebert-Sphere. Our results of the collapse in the isothermal and non-isothermal regime are given in Sec. 3. This sections includes also a review of the pure isothermal collapse of a overcritical Bonnor-Ebert-Sphere. The formation of disks in low and high mass rotating cores are discussed in Sec. 4 and in Sec. 5 we present our results on the formation of rings and bars in the disk and their possible fragmentation. Finally, we summarize and discuss our findings in Sec. 6.

2 NUMERICAL SCHEME AND INITIAL CONDITIONS

For our studies of collapsing gas clouds we used the FLASH code (Fryxell et al. 2000) which solves the coupled gravito-hydrodynamic equations on an adaptive mesh. FLASH is based on a block structured adaptive mesh refinement (AMR) technique which is implemented in the PARAMESH library (Olson et al. 1999). This AMR technique allows us to follow the core formation over more the ten orders of magnitude in density increase without violating the Truelove criterion (Truelove et al. 1997). For this purpose we implemented a new refinement criterion to the FLASH code which assures that the local Jeans length

$$\lambda_J = \left(\frac{\pi c^2}{G \rho} \right)^{1/2} \quad (1)$$

is at least resolved by $N > 4$ grid points, where, c , G , and ρ are the isothermal sound speed, the gravitational constant, and the local mass density, respectively. The runs we present in this work are performed with an even smaller Jeans number $J = \Delta x / \lambda_J$ of 1/8 or 1/12 (Δx is the grid spacing in one dimension at the point x).

2.1 Properties of Bonnor-Ebert-Spheres

We choose as an initial setup a non magnetized spherical gas cloud in a marginal stable hydrostatic equilibrium, i.e. a Bonnor-Ebert-Sphere (Ebert 1955; Bonnor 1956). With the definitions

$$\rho(\xi) \equiv \rho_0 e^{-\Phi(\xi)} \quad (2)$$

$$\xi \equiv \frac{r}{r_0} ; \quad r_0 = \frac{c}{\sqrt{4\pi G \rho_0}} \quad (3)$$

the radial density profile is given by the solution of the Lane-Emden equation (cf. Chandrasekhar 1967):

$$\frac{1}{\xi^2} \frac{d}{d\xi} \left(\xi^2 \frac{d\Phi}{d\xi} \right) = e^{-\Phi} \quad (4)$$

$$\Phi(0) = \Phi'(0) = 0 \quad (5)$$

where ρ_0 is the initial central density, c is the thermal sound speed, r_0 is the characteristic radius of the gas cloud, and a prime ($'$) denotes the differentiation with respect to ξ . The solution is characterized by a density profile with a flat core of density ρ_0 and an envelope which falls off with radius roughly as r^{-2} until truncated by the pressure of the surrounding medium. Note that the function $\phi(\xi)$ is – up to an integration constant – equal to the gravitational potential ψ (cf. Eq. (11)).

We use a fourth order Runge-Kutta numerical scheme to solve Eq. (4) for the potential $\phi(\xi)$, and the acceleration $\phi'(\xi)$ which give the density profile $\rho(\xi)$ and the mass parameter $q(\xi)$. Fig. 1 summarizes the radial dependences of the dimensionless parameters which determine the Bonnor-Ebert-Sphere with the cut-off radius of $\xi_c = 6.5$.

The total mass within a Bonnor-Ebert sphere at the radius ξ is given by

$$\begin{aligned} M(r) &= \frac{c^3}{\sqrt{4\pi G^3 \rho_0}} q \quad (6) \\ &\approx 1 M_{\odot} \left(\frac{T}{20 \text{ K}} \right)^{\frac{3}{2}} \left(\frac{\rho_0}{8 \times 10^{-17} \text{ g cm}^{-3}} \right)^{-\frac{1}{2}} \\ &\quad \times \left(\frac{q}{15.85} \right) , \end{aligned}$$

where q is the integrated dimensionless mass factor (see also McLaughlin & Pudritz 1996),

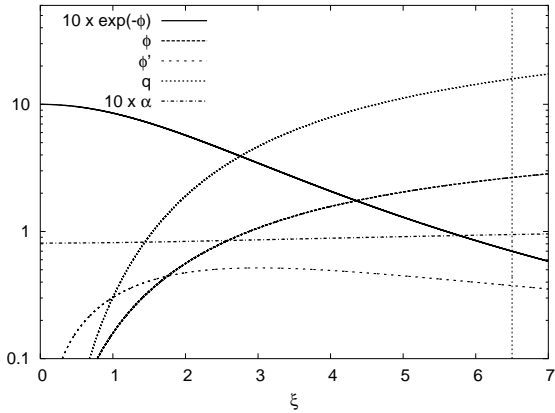


Figure 1. Shows the dimensionless parameters of a Bonnor-Ebert-Sphere: the density profile (solid line) multiplied by a factor of 10, the potential ϕ (dashed line), the gravitational acceleration ϕ' (thin dashed line), the mass parameter q (dotted line), and the ratio of the thermal energy to gravitational energy α (dash-dotted line) multiplied by a factor of 10 for a sphere with $\xi_c = 6.5$. The vertical line indicates this cut-off radius.

$$q = \xi^2 \Phi' \quad (7)$$

Such a sphere is unstable to collapse if its dimensionless radius ξ is larger than 6.451 (Bonnor 1956)¹. Given the external pressure P_{ext} and the sound speed of such a spherical cloud the physical radius and total mass are, respectively:

$$R = 0.49 \frac{c^2}{G^{1/2}} P_{\text{ext}}^{-1/2} \quad (8)$$

$$M = 1.18 \frac{c^4}{G^{3/2}} P_{\text{ext}}^{-1/2} \quad (9)$$

The ratio of thermal to gravitational energy, α , within a Bonnor-Ebert-Sphere, which varies only slightly with radius, is completely fixed by its truncation radius ξ_c . This can be seen by the following argument. The gravitational potential ψ inside the sphere is determined by

$$\frac{d\psi}{dr} = G \frac{M}{r^2}, \quad (10)$$

where the mass M is given by Eq. (7). Using the matching conditions at the edge of the sphere with the potential in the ambient media, i.e. $\psi \propto r^{-1}$ for $\xi > \xi_c$, the solution of Eq. (10) is

$$\psi = -c^2 [\phi_c + q_c - \phi] \quad \text{for } \xi \leq \xi_c, \quad (11)$$

where $\phi_c \equiv \phi(\xi_c)$, $\phi'_c \equiv \phi'(\xi_c)$, and $q_c \equiv q(\xi_c)$. Therefore, $\alpha = 3/2 c^2/|\psi|$ is given by

$$\alpha = \frac{3}{2} \frac{1}{\phi_c + q_c - \phi} \quad (12)$$

With $\xi_c = 6.5$ ($\phi_c = 2.66$, $q_c = 15.85$) α is in the range of:

$$0.081 \leq \alpha \leq 0.094 \quad (13)$$

The rotational to gravitational energy β for a rigidly rotating Bonnor-Ebert-Sphere is given by

$$\beta = \frac{2}{5} \frac{v_\phi^2}{c^2} \frac{1}{\phi_c + q_c - \phi} = \frac{16}{15\pi^2} \frac{\xi^2 (t_{\text{ff}} \Omega)^2}{\phi_c + q_c - \phi}, \quad (14)$$

¹ Note, as $\xi = 2\pi r/\lambda_J$ this instability criterion is almost equal to Jeans' instability criterion, i.e. $r > \lambda_J$, and the amount of Jeans masses within the sphere is $3/\pi^3 q \sim 1.53$.

run	t_{ff} [s]	Ω [rad s ⁻¹]	$t_{\text{ff}} \Omega$	β_{max}
A1	3.63×10^{13}	2.755×10^{-15}	0.1	2.88×10^{-3}
A2	3.63×10^{13}	5.509×10^{-15}	0.2	1.15×10^{-2}
A3	3.63×10^{13}	8.265×10^{-15}	0.3	2.59×10^{-2}
B68	2.12×10^{12}	9.430×10^{-14}	0.2	1.21×10^{-2}

Table 1. The initial parameters for the simulations we present in this paper. Where Ω , t_{ff} , and β_{max} are the initial angular velocity, the initial free fall time, and the maximum of ratio of the rotational and gravitational energy, respectively.

where v_ϕ and Ω are the toroidal velocity and angular velocity, respectively. For instance, a sphere rotating with $t_{\text{ff}} \Omega = 0.1$ has values of β that span the range

$$0 \leq \beta \leq 0.0029 \quad ; \quad (15)$$

and scales roughly proportional to ξ^2 , while β takes its maximum at the edge of the sphere and is given by $\beta_{\text{max}} = 0.11 (\phi'_c)^{-1} (t_{\text{ff}} \Omega)^2$.

2.2 Initial conditions: low and high mass cores

In this paper we present the results of four simulations aiming to study both low and high mass pre-stellar cores. We start each simulation with an overcritical Bonnor-Ebert-Sphere which rotates initially with a constant angular velocity Ω . Three of these initial models have the same initial core density ρ_0 but different initial angular velocities Ω (run A1 – A3) and a mass of $168 M_\odot$ characteristic of massive star formation (Chini et al. 2004), and one low mass model starting with a core density according to the observed Bok globule Barnard 68 by Alves et al. (2001) with a mass of $2.1 M_\odot$ and a medium angular velocity (run B68). The initial parameters of these runs are summarized in table 1.

One particularly interesting object for low mass star formation is the Bok globule Barnard 68 which was extensively studied by Alves et al. (2001). The density profile of this cloud exhibits a close to perfect Bonnor-Ebert profile with $\xi_c = 6.9 \pm 0.2$ corresponding to a physical radius $R = 1.25 \times 10^4$ AU, a core density of $\rho_0 = 1.0 \times 10^{-18}$ g cm⁻³, a total mass of $M_{\text{B68}} = 2.1 M_\odot$, and a temperature of $T = 16$ K (we set up this run with an external pressure of $P_{\text{ext}}/k_B = 2.4 \times 10^5$ K cm⁻³). This corresponds to model marked by a diamond shown in Fig. 2. One can see that this observed system is nearly immediately scalable from the initial state that we use defined by the triangle. To simulate the collapse of a realistic molecular cloud we initialize run B68 with the physical parameters given above. According to Lada et al. (2003) Barnard 68 might rotate slightly with a ratio of the rotational to gravitational energy of a few percent. We initialize the sphere with $t_{\text{ff}} \Omega = 0.2$ corresponding to $\beta_{\text{max}} \approx 0.01$.

Most of our simulations are designed to study the formation of massive accretion disks in which massive (O, B) stars may form. The collapse of massive (up to $120 M_\odot$), initially singular cores has been simulated by Yorke & Sonnhalter (2002) who included a careful treatment of radiative transfer effects. Recent observations by Chini et al. (2004) have discovered a massive ($20 M_\odot$) star that is being formed within a very massive, large accretion disk (at least $100 M_\odot$ of gas) in the young star forming region of M 17. We therefore chose the initial setup for the study of massive star and disk formation corresponding to runs A1 – A3 as

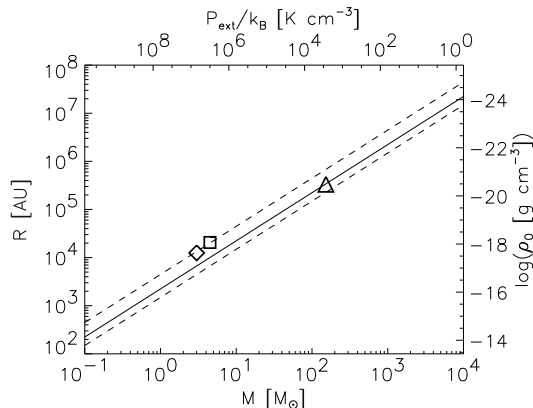


Figure 2. Scaling of the physical parameters of critical Bonnor-Ebert-Spheres. The solid line shows the parameters for sphere with $T = 20$ K, and the upper and lower dashed lines show the relations for a sphere with $T = 10$ K and $T = 30$ K, respectively (Note that the axis labeling for P_{ext} is only valid for $T = 20$ K and has to be rescaled for different temperatures). The triangle (Δ) refers to our model parameters for A1 – A3, the square (\square) shows the Coalsack globule 2 observed by Racca et al. (2002), and the diamond (\diamond) marks the properties of Barnard 68 (our model B68) as given in Alves et al. (2001).

follows: the cut-off radius is $\xi_c = 6.5$ corresponding to a physical radius of $R = 1.62$ pc ($R = 3.34 \times 10^5$ AU), an unperturbed core density $\rho_0 = 3.35 \times 10^{-21}$ g cm $^{-3}$, and sound speed $c = 0.408$ km s $^{-1}$ ($T = 20$ K). This parameters with a 10% overdensity result in a total mass of the gas cloud of $M = 168 M_\odot$, and an external pressure $P_{\text{ext}}/k_B = 3.2 \times 10^3$ K cm $^{-3}$. The initial free fall time $t_{\text{ff}} = \sqrt{3\pi/32 G \rho_0}$ of our Bonnor-Ebert sphere is 1.1×10^6 years 2 . The edge of the sphere is defined by a density decrease of the ambient medium by a factor of 100 whereas the pressure is continuous at the edge of the sphere. Therefore, the ambient low density gas is a hundred times warmer ($T_{\text{amb}} = 2000$ K) than the cold gas cloud and the sound speed there is $c_{\text{amb}} = 4.08$ km s $^{-1}$. To make sure that the evolution of the sphere is not influenced by the simulation box boundaries we choose the simulation volume to be $(100 r_0)^3 \sim (15 R)^3 \sim (25 \text{ pc})^3$.

Fig. 2 shows the scaling relations in the isothermal regime for the physical mass, radius, core density, and external pressure for critical Bonnor-Ebert-Spheres. All spheres at a given temperature with the properties indicated by the shown lines are equivalent.

Radiative cooling by molecular excitation lines is very efficient in the low density regime. In fact, molecular clouds will maintain the same temperature during their collapse until the density rises above $n \sim 10^7$ cm $^{-3}$. We wish to study this transition to less efficient cooling very carefully and therefore start the collapse of Bonnor-Ebert-Spheres in this low-density, isothermal phase. Therefore, we choose the initial density for the runs A1 – A3 ($n_0 \sim 10^3$ cm $^{-3}$) in order to sample the full range of densities given by the cooling data of Neufeld & Kaufman (1993) and Neufeld et al. (1995). Their cooling data span a number density of $10^3 \leq n(H_2) \leq 10^{10}$ cm $^{-3}$. We emphasize however that these initial physical conditions can be rescaled only as long as the gas stays at the same temperature, i.e. contracts isothermally (cf. dis-

cussion in section 3). Therefore, we can apply our results to observed molecular clouds with different initial physical parameters.

All runs are set up with a 10% $m = 2$ density perturbation on top of a slightly enhanced Bonnor-Ebert-Profile, i.e.,

$$\rho = \rho_{\text{BE}} (1.1 + 0.1 \cos(2\varphi)) \quad , \quad (16)$$

where ρ_{BE} obeys Eq. (4) and φ is the azimuthal angle (the 10% overall density enhancement guarantees the collapse of a critical BE-sphere since it overwhelms the relatively small amount of rotation). All spheres rotate initially with a rigid body rotation profile with the amount of rotation given in table 1.

2.3 Radiative cooling

Earlier (for a review see Bodenheimer et al. 2000) and recent (e.g. Matsumoto & Hanawa 2003) simulations of protostellar disk formation and fragmentation typically use two types of equations of state: (i) an isothermal equation of state throughout, which assumes that radiative cooling is always efficient enough to keep the gas at the same initial temperature, or (ii) an isothermal EOS that is switched to an adiabatic one at sufficiently high density. We did some simulations of the latter approach and found problems not only due to numerical artifacts but also due to physical difficulties because the sudden change of the equation of state violates energy conservation (an isothermal EOS corresponds to an infinite heat bath whereas an adiabatic EOS assumes a finite thermal energy).

To achieve a more realistic, and more physically correct picture of the formation of protostellar disks, we account in our simulations for the effect of cooling by collisional excitations of gas molecules. We use cooling functions provided by Neufeld & Kaufman (1993); Neufeld et al. (1995). These authors computed the radiative cooling rates as a function of the gas temperature, density and optical depth for the temperature and density range of $10 \leq T \leq 2500$ K and $10^3 \leq n(H_2) \leq 10^{10}$ cm $^{-3}$. Using steady state molecular abundances for the most important coolants in molecular clouds (H_2 , H_2O , CO, O_2 , HCl, C, and O) they provide a total cooling rate which can be used to calculate the energy loss due to radiative cooling. We use their optical depth parameter for a singular isothermal sphere (which is appropriate for a sphere with a $1/r^2$ density profile)

$$\tilde{N}_{\text{SIS}} = 5.1 \times 10^{19} \left(\frac{n}{\text{cm}^{-3}} \right)^{1/2} \text{ cm}^{-2} \text{ per km s}^{-1} \quad (17)$$

to read off the total cooling rate from the provided cooling data base. The cooling rates provided by Neufeld & Kaufman (1993) and Neufeld et al. (1995) are available for densities $n(H_2) \leq 10^{10}$ cm $^{-3}$. Because the cooling power per H_2 molecule in the high temperature ($T > 100$ K) and high density ($n > 10^{10}$ cm $^{-3}$) regime is nearly independent of the density, we extrapolate their data in the high density range assuming that the cooling power is only a function of temperature. As the maximum temperatures in our simulations are well below the dissociation temperature of H_2 ($T_{\text{diss}} \sim 2000$ K) we do not account for this cooling process in the present simulations. We also did not consider cooling processes due to gas-grain interactions which we will implement in future studies. However, our results are similar in character to those of Yorke et al. (1995) who did include dust cooling.

The treatment of the thermal cooling of the gas allows one to calculate the internal energy density, ϵ , at any position and time. The pressure, P , at each time step is then calculated by:

$$P = \epsilon(1 - \gamma) \quad , \quad (18)$$

² Note that the more accurate dynamical time scale for a Bonnor-Ebert-Sphere is $t_0 = 1/\sqrt{4\pi G \rho_0} \approx 0.52 t_{\text{ff}}$

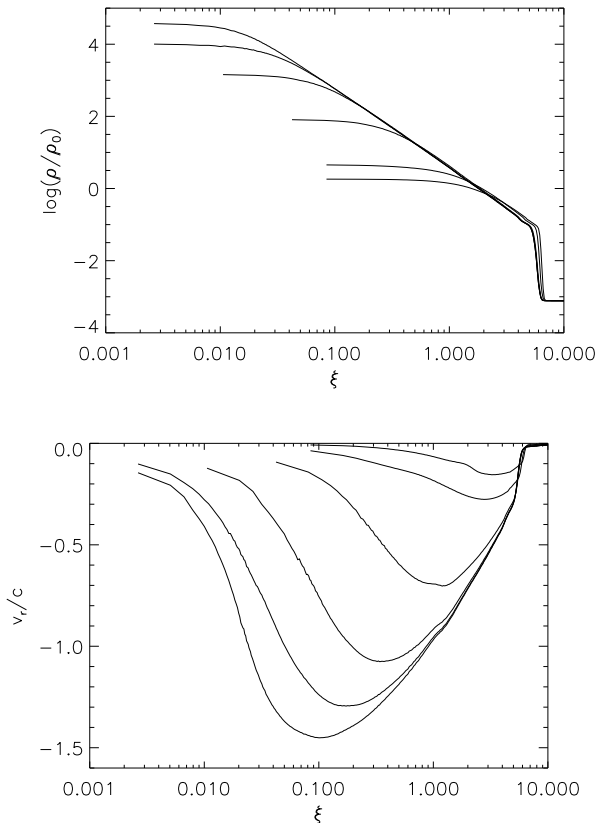


Figure 3. Radial profiles of density (first panel) and the radial velocity (second panel) at different times in the isothermal regime. The sphere starts to collapse from *outside-in* leaving a $1/r^2$ density profile in the envelope while the flat core region shrinks. The maximal infalling velocity appears close to the edge of the core and is moving inward with increasing density. The shown lines correspond to (from bottom to top of the first panel, and top to bottom for the second panel) $t/t_0 = 3.7, 5.6, 7.13, 7.33, 7.36, 7.37$, where $t_0 = 1/\sqrt{4\pi G \rho_0} \sim 6.0 \times 10^5$ years and the data are taken from run A1.

where γ is the adiabatic index. Throughout this study we use a constant γ of $5/3$. Including cooling in our simulations the thermal energy is not only altered by compressional heating during the collapsing phase but also by the loss of energy due to radiative emission. We found it is useful to compare our approach which uses full molecular cooling, with the earlier adiabatic model studies by calculating an effective EOS, i.e. $\gamma_{\text{eff}} \equiv dP/d\rho$, at each time step.

3 CORE FORMATION AND EVOLUTION

3.1 Pure isothermal collapse of Bonnor-Ebert-Spheres

Early theoretical work on star formation (e.g. Hayashi & Nakano 1965) already pointed out that cooling during the initial stage of collapsing molecular cloud cores is efficient enough to ensure constant temperatures of the gas over 4 – 5 orders of magnitude in density increase. Hence, the isothermal collapse proceeds as a free falling contraction of the gas. Our simulations – including molecular cooling – resemble this early isothermal phase until $n \sim 10^{7.5} \text{ cm}^{-3}$. Fig. 5 and Fig. 7 from our simulation A1 clearly show the evolution in the isothermal phase at low densities. Be-

cause the solutions of collapsing isothermal Bonnor-Ebert-Spheres are rather general we devote the following paragraph to review the collapse of a pure isothermal cloud.

A detailed 1D numerical investigation of a collapsing isothermal Bonnor-Ebert-Sphere was done by Foster & Chevalier (1993). The results of our 3D simulations in the isothermal regime are very similar to the results found by Foster & Chevalier (1993). Fig. 3 shows the time evolution of the density profile and the radial velocity profile which have the same trend as the 1D results: after a sound wave propagates through the sphere at a sound crossing time of $t_{\text{sc}} = \xi/\sqrt{4\pi G \rho_0}$ ($\sim 3.8 \times 10^6$ years in the case of runs An and $\sim 2.4 \times 10^5$ years in the case of B68) the cloud starts to collapse from *outside-in*. Initially the gravitational acceleration of the Bonnor-Ebert-Sphere

$$g = \frac{GM}{r^2} = c \sqrt{4\pi G \rho_0} \phi' \quad (19)$$

is largest at $\xi = 3.0$, ($\phi'(3.0) = 0.517$), and decreases only slightly with radius ($\phi'(6.5) = 0.375$). Soon after the low density material from the outer part of the cloud is accelerated towards the center the density profile of the sphere starts to change: a high density flat core with a $1/r^2$ envelope builds up. The $1/r^2$ law in the envelope reflects the fact that the sphere maintains a state that is close to hydrostatic equilibrium in the envelope. Now the gravitational acceleration is highest at the edge of the flat core and decreases with $1/r$. Therefore, material at the core boundary is constantly accelerated whereas material in the envelope stays nearly at a constant infalling velocity because the acceleration becomes very low in this region. As the core density increases the core shrinks continuously and the $1/r^2$ envelope profile becomes more dominant. The maximum of the radial velocity appears around the edge of the flat core region and is moves inward with time. Although, the infalling material becomes supersonic, no shock occurs in this isothermal collapsing phase since the central gravitational force accelerates the gas in front of the supersonic material fast enough to prevent a velocity discontinuity. The radial velocity stays close to zero at the outer edge of the sphere and at the center of the cloud.

We emphasize that the collapse of an over-critical Bonnor-Ebert-Sphere differs from the Expansion-Wave solution of Shu (1977) since the latter is an inside-out collapse of an initially singular isothermal sphere (SIS). The collapse of a SIS proceeds in a self-similar fashion leading to a velocity profile that increases with decreasing radial distance to the center (cf. Fig. 2 of Shu 1977) whereas the velocity of a collapsing Bonnor-Ebert-Sphere possesses always a finite maximum and goes to zero at the center of the sphere.

To get a quantitative estimate of the isothermal collapse described above we approximate the density profile shortly after the initial collapse by:

$$\rho(r) \approx \begin{cases} \rho_{\text{core}} & : r \leq r_{\text{core}} \\ \rho_{\text{core}} (r/r_{\text{core}})^{-2} & : r \gg r_{\text{core}} \end{cases} \quad (20)$$

where ρ_{core} is the core density and r_{core} is the radial distance to the core edge. This approximation is valid as long as the collapse is isothermal. The core becomes non-isothermal after the density increased above the critical density of $n \sim 10^{7.5} \text{ cm}^{-3}$ (see section 3.2).

Using conservation of the mass of the sphere M we can estimate the core radius for a given core density (with the critical density of $\rho_{\text{core}} = 10^{-16} \text{ g cm}^{-3}$ and a sound velocity of

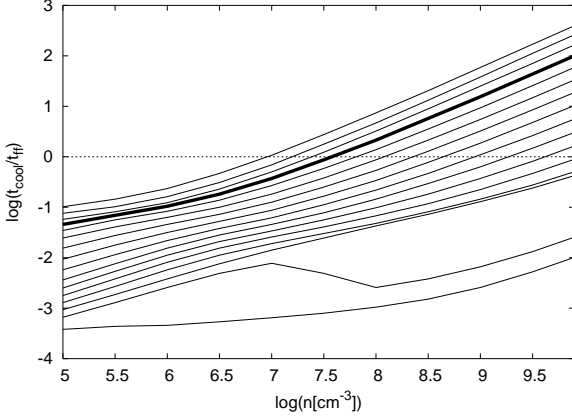


Figure 4. Comparison of the local free-fall time t_{ff} with the cooling time t_{cool} in different temperature regimes. For a 20 K cloud (thick line) the cooling time becomes longer than the free-fall when its number density exceeds $n \approx 10^{7.6} \text{ cm}^{-3}$. The cooling data are taken from Neufeld et al. (1995) and Neufeld & Kaufman (1993). The temperature range is $T = 10 \text{ K} - 10^{2.5} \text{ K}$ (from top to bottom) in steps of 0.1 dex.

$c = 0.41 \text{ km s}^{-1}$);

$$r_{\text{core}} \approx \sqrt{\frac{M}{4\pi \rho_{\text{core}} R}} = \frac{c}{\sqrt{4\pi G \rho_{\text{core}}}} (\xi_c \phi'_c)^{1/2}, \quad (21)$$

$$\sim 4.5 \times 10^2 \text{ AU}$$

where R is the radius of the sphere and we assumed $r_{\text{core}} \ll R$. Using this approximations the total core mass is given by

$$M_{\text{core}} \approx \frac{4\pi}{3} r_{\text{core}}^3 \rho_{\text{core}} = \frac{1}{3} M \frac{r_{\text{core}}}{R}$$

$$= \frac{1}{3} \frac{c^3}{\sqrt{4\pi G^3 \rho_{\text{core}}}} (\xi_c \phi'_c)^{3/2} \quad (22)$$

$$\sim 0.1 M_{\odot}.$$

3.2 Collapse with molecular cooling: initial isothermal phase

Theoretical models of collapsing protostars predict that the formation of a protostar occurs in several stages (e.g. Larson 1969, 2003). Already from Fig. 4, which compares the cooling time scale t_{cool} and the local free fall time t_{ff} , one can infer that a gravitationally unstable low density cloud will undergo a isothermal collapse until the cooling by molecular line emission becomes inefficient when $t_{\text{cool}} > t_{\text{ff}}$. For instance, a 20 K cloud cannot be efficiently cooled if its core density exceeds more than $10^{7.6} \text{ cm}^{-3}$. After the core density reaches this critical value, the high density region of the gas cloud contracts almost adiabatically on a much longer time scale. Another prediction one can infer from Fig. 4 is the evolution trajectory of the core in the temperature-density-plane which follows the track where $t_{\text{ff}} \sim t_{\text{cool}}$ in the inefficient cooling regime. Our simulations are in good agreements with this prediction.

Initially, due to effective cooling, the unstable sphere maintains its initial temperature while collapsing on its local free fall time. Fig. 5 shows the evolution trajectory of the cloud's core in the temperature-density plane from our simulation A1. The initial contraction stage clearly indicates the regime where cooling is fast enough to stay at the clouds initial temperature while core density increases. A quantification of this stage is shown in Figs. 6 and 7 where we compute the effective equation of state, i.e.

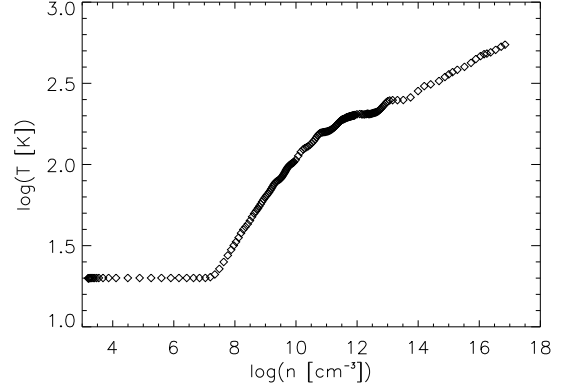


Figure 5. Evolution trajectory of the core forming region from our simulation in the temperature-density plane. Initially, the core undergoes a rapid isothermal contraction until the cooling by molecular lines becomes inefficient, i.e. $t_{\text{cool}} > t_{\text{ff}}$, at a core density $n_{\text{core}} \sim 10^7 \text{ cm}^{-3}$ (from run A1).

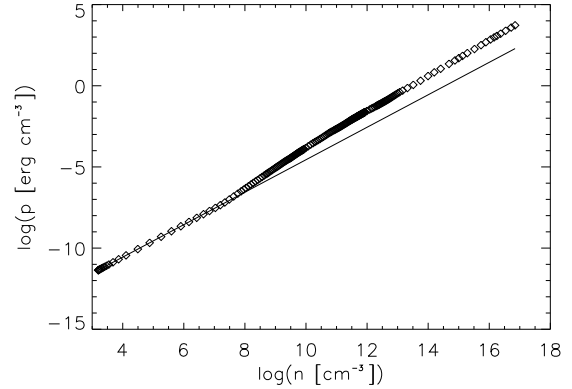


Figure 6. Shows the thermal pressure, $P = P(n_{\text{core}})$, in the core forming region. The initial isothermal collapse (indicated by the solid line, $p \propto n$) is followed by a non-isothermal contraction with a non-linear pressure response (from run A1).

$\gamma_{\text{eff}} \equiv d \log p / d \log \rho$. We calculate the trajectory plots by averaging the variables in the region where $n_{\text{max}}/2 \leq n \leq n_{\text{max}}$, where $n_{\text{max}}(t)$ is the maximal density in our simulation at the time t where $n_{\text{max}}(t)$ increases continuously with time.

From Fig. 4 and from our simulations (Fig. 5 and Fig. 7) we get a core density (i.e. of material interior to radius r_{core}) at the end of the isothermal phase of $n_{\text{core}} \sim 10^{7.5} \text{ cm}^{-3}$ and $\rho_{\text{core}} \sim 10^{-16} \text{ g cm}^{-3}$. Using Eq. (21) and Eq. (22) gives a core radius of $r_{\text{core}} \sim 450 \text{ AU}$ and a core mass of $M_{\text{core}} \sim 0.1 M_{\odot}$. Note that these values are independent of the initial mass M and radius R as long as the initial sphere obeys the Bonnor-Ebert profile given by Eq. (4). Other investigations of spherical collapses of molecular clouds (for a review see Larson 2003) also predict a first 'hydrostatic core' when the density reaches $\sim 10^{-10} \text{ g cm}^{-3}$ where the core mass is almost independent of the clouds initial mass or radius. The predicted 'hydrostatic core' mass is about $0.01 M_{\odot}$. Our findings give a larger core mass at the end of the isothermal collapsing phase as cooling becomes inefficient at lower densities.

Comparing the value of the core mass at the end of the isothermal phase to the local Jeans mass, $M_J = \pi^{5/2} / 6 c^3 / \sqrt{G^3 \rho_{\text{core}}} \approx$

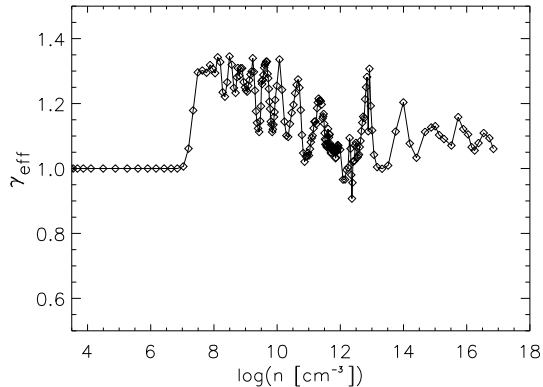


Figure 7. The effective equation of state, $\gamma_{\text{eff}} = d \log p / d \log \rho$, in the core forming region as a function of the core density (from run A1).

$0.56 M_{\odot}$, (which is independent of the sphere parameters) gives an estimate of gravitational strength at this point. The fact that $M_{\text{core}}/M_J < 1$ in the fast contracting isothermal phase is the reason that the collapsing cloud has not yet broken up into several fragments.

With the approximation of the radial density profile Eq. (20) the total mass within a sphere of radius $r \gg r_{\text{core}}$ is given by

$$\begin{aligned} M(r) &\approx \frac{c^2}{G} (\xi_c \phi'_c) r \\ &\approx 1 M_{\odot} \left(\frac{T}{20 \text{ K}} \right) \left(\frac{r}{3.3 \times 10^{16} \text{ cm}} \right), \end{aligned} \quad (23)$$

where we used $\xi_c = 6.5$ for the numerical example. Comparing the core mass M_{core} to total mass of the sphere, M , we get

$$\begin{aligned} \frac{M_{\text{core}}}{M} &\approx \frac{1}{3} \left(\frac{\phi'_c}{\xi_c} \right)^{1/2} \left(\frac{\rho_{\text{core}}}{\rho_0} \right)^{-1/2} \\ &\approx 0.08 \left(\frac{\rho_{\text{core}}}{\rho_0} \right)^{-1/2}. \end{aligned} \quad (24)$$

Using Eq. (23) we can compute the mass accretion at different radii:

$$\dot{M}(r) \approx -\frac{c^2}{G} (\xi_c \phi'_c) v_r, \quad (25)$$

where v_r is the radial infall velocity. The gravitational acceleration outside the core region is $g \approx c^2 (\xi_c \phi'_c) / r$ and the radial velocity $v_r \approx c^2 (\xi_c \phi'_c) (4\pi G \rho_{\text{core}})^{-1/2} / r$ assuming that the velocity changes on the dynamical time of the core region³. Together with the size of the core region Eq. (21) we get a good estimate of the mass accretion onto the core:

$$\begin{aligned} \dot{M}_{\text{core}} &\approx \frac{c^3}{G} (\xi_c \phi'_c)^{3/2} \\ &\sim 6.1 \times 10^{-5} M_{\odot} / \text{year} \left(\frac{T}{20 \text{ K}} \right)^{3/2} \end{aligned} \quad (26)$$

³ This assumption predicts a r^{-1} dependence of the radial velocity outside the core region. Our simulations show only a weak dependence of the velocity on the radius. Using the *local* dynamical time gives a velocity which is independent of r . From our simulations we conclude that the increase of the infall velocity occurs on a time scale somewhat in between the dynamical time and the local free fall time. Using either time scale give the same velocity and mass accretion at the core edge.

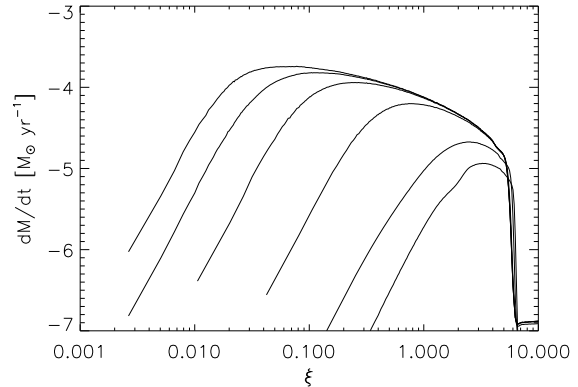


Figure 8. Spherical averaged radial profiles of the mass accretion in the isothermal regime corresponding to Fig. 3. The maximum mass accretion occurs roughly at the core radius r_{core} which moves steadily towards the center (from run A1).

Eq. (26) shows that the mass accretion of a collapsing Bonnor-Ebert-Sphere is independent of its initial mass and radius. This result is applicable to non-merging, i.e. low mass, cloud cores and similar to the case of a collapsing SIS (Shu 1977).

Although Eq. (26) suggests that the mass accretion is constant in time we observe a slowly increasing \dot{M} which is due to the steady increase of the radial velocity. At a given radius $r \gg r_{\text{core}}$ in the envelope the mass accretion approaches a constant value. The mass accretion has its maximum at the at the core radius and drops quickly towards the core center as the radial velocity sharply at radii $r < r_{\text{core}}$ Fig. 8 shows the evolution of the mass accretion in the isothermal regime.

3.3 Collapse with cooling: post-isothermal phase

When the central density exceeds the critical density $n_{\text{crit}} \approx 10^{7.5} \text{ cm}^{-3}$ thermal energy produced by gravitational contraction is no longer radiated efficiently and the core starts to heat up. The resulting increase of the thermal pressure slows down the contraction of the central gas region and the effective equation of state becomes stiffer. This is reflected in the increase of the effective equation of state, γ_{eff} . Our simulations (cf. Fig. 7) show a steep increase of γ_{eff} from 1.0 to ≈ 1.3 after the core density rises above the critical cooling density. Due to the complex cooling process γ_{eff} does not stay at a fixed value but varies with time with a trend to decrease in the regime $10^8 \lesssim n_{\text{core}} \lesssim 10^{12} \text{ cm}^{-3}$. The strong variability of γ in Fig. 7 reflects also the multiple shock occurrence during the collapse (cf. Fig. 19). Note also that the data points in this plot do not correspond to the time steps in the simulation but to the larger time steps at which we got output data files. Sampling the data points on a higher time resolution might result in a smoother graph.

In the post-isothermal phase, the density increase in the center of the gas cloud is dictated by the cooling time t_{cool} as opposed to the dynamical time t_{ff} . Fig. 9 shows the evolution time scale of the core region, i.e. $n_{\text{core}}/\dot{n}_{\text{core}}$ as a function of the density. After the core density reached $\sim 10^8 \text{ cm}^{-3}$ the collapse proceeds on a time scale that is determined by cooling process. At densities of $\gtrsim 10^{10} \text{ cm}^{-3}$ the core density increases on a nearly constant time scale much larger than the local free fall time marking a phase of ‘hydrostatic equilibrium’ (cf. also Larson 1969). At later times the

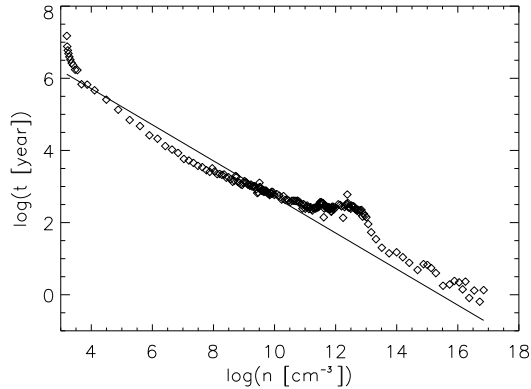


Figure 9. Evolution time scale, $t_{\text{evol}} \equiv n_{\text{core}}/\dot{n}_{\text{core}}$, as a function of the core density n_{core} . The solid line shows the local free-fall time, i.e. $t \propto n_{\text{core}}^{-1/2}$ (from run A1).

temperature of the core (at $n \gtrsim 10^{13} \text{ cm}^{-3}$ and $T \gtrsim 250 \text{ K}$) rises to a point when cooling by molecular excitations becomes more efficient (due to the abundant production of H_2O and its multitude of excitation levels) and the collapse proceeds again almost on the local free fall time.

The slower contraction of the warmer core region, as compared to the isothermal case, causes the supersonic infalling material to shock at the edge of the warm core. These first shocks occur preferentially above and below the disk plane where the gas is not rotationally supported at a typical distance of $\sim 650 \text{ AU}$ (for the runs A_n) from the center. Temperatures at this point reach $70 - 80 \text{ K}$ and the temperature profile is discontinuous rising from 30 K to 70 K between the outer pre-shock region and the shocked region within a few tens of AU (cf. Fig. 10). The velocities at this point reach values of 1.5 km s^{-1} ($\mathcal{M} \approx 2.5$). As infalling gas piles up at the shock boundary, a density discontinuity also develops in the post-shock region which separates a low density envelope and a high density pre-protostellar disk. This post-shock region slowly moves towards the center of the gas cloud and its temperature increases further while supersonic gas from the outside envelope hits this shock boundary.

Gas inside this first shock region is subsonic and therefore not shock heated leading to a lower temperature region behind the shock. As the core density and the core temperature continue to increase, gas inside the pre-protostar region becomes supersonic and a secondary shock develops at $\sim 100 \text{ AU}$ above and below the disk plane (cf. second panel of Fig. 10). Typical temperatures at the secondary inner shock boundaries are $\sim 150 \text{ K}$ whereas the core stays cooler. This stage (the core density is now $\sim 10^{11} \text{ cm}^{-3}$) marks the first development of the protostellar disk.

Similar to the outer first shock, the inner shock fronts move slowly towards the disk plane while the local Mach number rises to $\mathcal{M} \sim 4$ corresponding to a shock velocity of 3 km s^{-1} . Again, the collapsing core region is fed only by gas inside the inner shock fronts whereas gas falling from outside onto the shocks is stalled at the shock boundaries and heats up the gas in these shock regions.

Fig. 11 shows the time evolution of the density profile and temperature profile, respectively, in the non-isothermal regime from simulation A1. The second line from the bottom in the density plot marks the last stage of the isothermal collapse phase. In the non-isothermal phase the density profile deviates from the r^{-2} profile because of the slower contraction of the core during this regime.

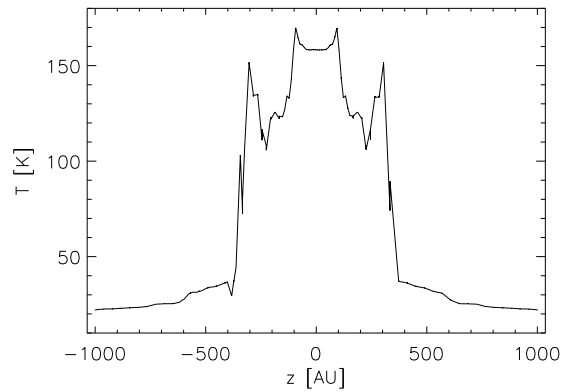
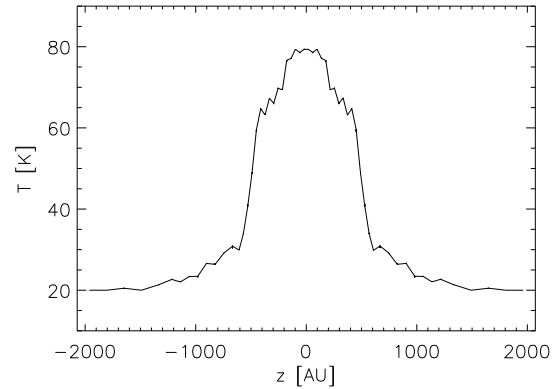


Figure 10. Temperature line profiles along the z -axis through the center of the gas cloud for run A1. The first panel shows the line profile after the first shock develops when the central density reached $2 \times 10^9 \text{ cm}^{-3}$. The second panel shows the temperature profile at a later stage when $n_{\text{core}} \sim 10^{11} \text{ cm}^{-3}$. At this time a second shock in the inner core region develops when supersonic material falls onto the protoplanetary disk (from run A1).

The density falls off more steeply than r^{-2} with increasing radius in the heated up region and approaches a r^{-2} profile in the isothermal regime at $r \gtrsim 10^{-16} \text{ cm}$. The transition region appears at a radius of $\sim 7 \times 10^{15} \text{ cm}$ which is in good agreement with the theoretical prediction of Eq. (21). The temperature profile rises steeply with decreasing radius, roughly as r^{-2} , whereas the core region has a flat temperature profile. The profiles $\rho(r)$ are radially bin-averaged spherical averages, i.e. $\rho(r) = \int d\Omega \rho(\mathbf{x})$, where $d\Omega = d\cos\theta d\varphi$ is the differential solid angle.

Fig. 12 shows the evolution of radial infall velocity as a function of radius from run A1. The peak velocity increases with time and 'moves' towards smaller radii (the first line from the top refers to the second line from the bottom of Fig. 11 which marks the end of the isothermal regime). Due to the shock which develops at the edge of the core the velocity profile becomes steeper with time whereas the peak velocity approaches a constant value of $\sim 3c$ in the spherical collapse phase. The velocity at the center drops always to zero.

In Fig. 13 we show the evolution of the 1D density profiles for run B68. Because the initial core density ρ_0 in this case is higher than for the runs A1 – A3 ($\rho_{\text{B68}}/\rho_{\text{A1}} \sim 300$) the isothermal region with $\rho \propto r^{-2}$ is smaller but the kink in the profile which separates the non-isothermal core region from the isothermal envelope appears at the same physical radius of $\sim 7 \times 10^{15} \text{ cm}$. This result is

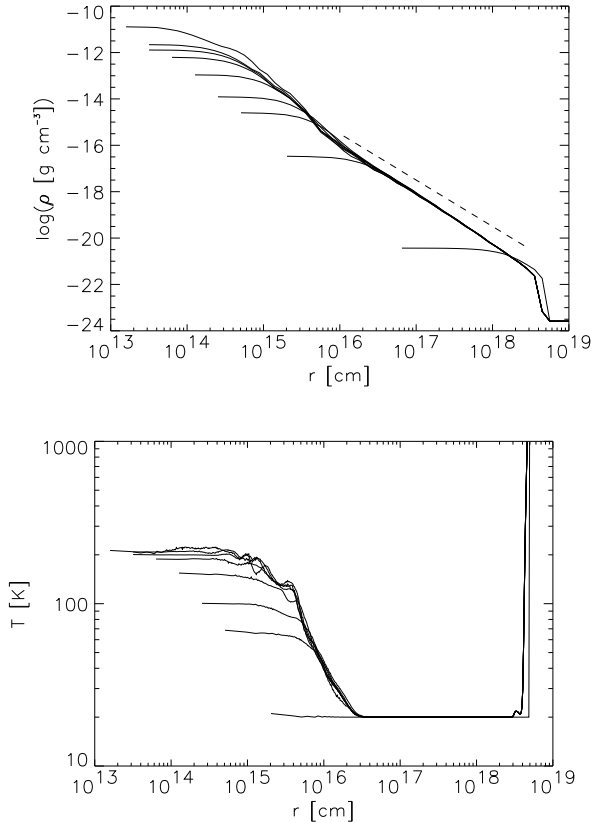


Figure 11. Radial profiles of the density (upper panel) and temperature (lower panel) at different times. As the simulation resolution increases with time due to the Jeans refinement criterion the shown line profiles also increase in resolution. The dashed short line shows a r^{-2} density profile. The data are compiled from run A1.

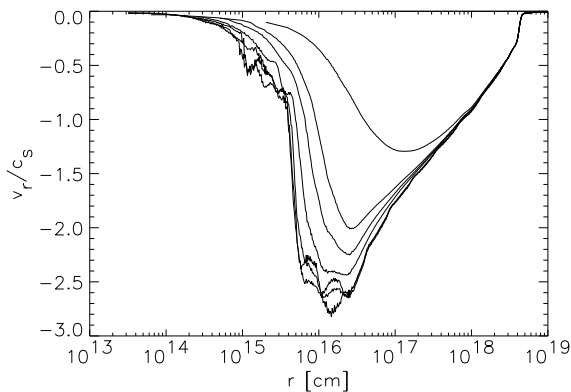


Figure 12. Radial profiles of the radial velocity at different times (this profiles correspond the those shown in Fig. 11). During the first stages of the spherical collapse the radial velocity increases steadily with time until it reaches the maximum value of $\sim 3c$ and the peak velocity is moving towards the inner part of the cloud. After the temperature in core region begins to increase the maximum of the radial Mach number stays at $r \sim 10^{16}$ cm (from run A1).

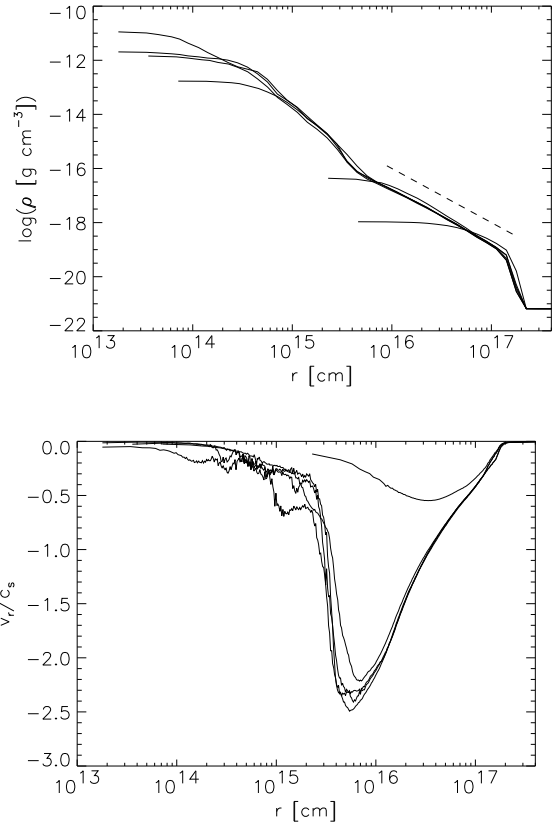


Figure 13. Similar to figures Fig. 11 and Fig. 12 except that the profiles are for run B68. The dashed line in the density panel shows a r^{-2} profile.

again in agreement with the theoretical prediction. Finally, we note that a similar double shock structure has been seen in 2D collapse simulations by Yorke et al. (1995) that feature dust as the coolant.

4 DISK FORMATION

As described in the previous section, the appearance of the secondary shock establishes the initial state for the formation of the protostellar disk. The protostellar disk builds up and achieves a column density of $\Sigma \approx 10^{1.5} \text{ g cm}^{-2}$ and a disk height $h \sim 200 \text{ AU}$. As the shock fronts move towards the equatorial plane, the density and temperature increase on a time scale slower than the local free fall time. Fig. 14 (run A1) and Fig. 17 (run B68) show the time evolution of the column density which we compute as follows:

$$\Sigma(R) \equiv \int dz \rho(x, y, z) \quad . \quad (27)$$

where $R = \sqrt{x^2 + y^2}$ is cylindrical radius and we evaluate the integral (27) throughout the entire simulation box. Similar to the radial density profile the column density profile develops a envelope and a flat core region. The non-isothermal core is separated from the envelope by a steep increase in density which leads to a kink in the radial density profile. In general, we find that the column density falls off roughly as r^{-2} . The disk height decreases while the disk gets denser and reaches a value of $\sim 10 \text{ AU}$ when the column density becomes $\sim 10^3 \text{ g cm}^{-2}$.

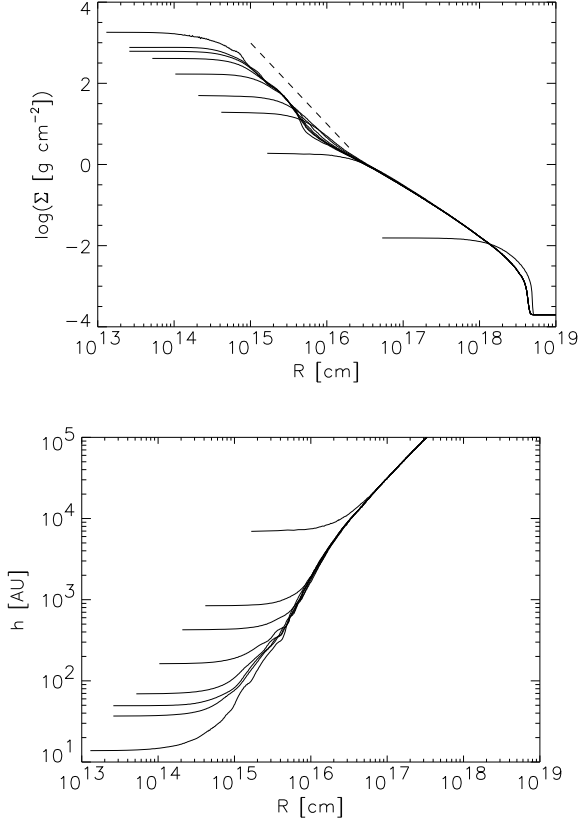


Figure 14. Radial profiles of the column density Σ and disk height h at different times. For comparison, the dashed line shows a R^{-2} profile. The shown profiles correspond to the density shown in Fig. 11 (run A1).

In the case of run B68 the ring structure is clearly visible in latest density profile.

Once a disk-like object forms, one can define the disk height h by

$$h(R) = \frac{\Sigma(R)}{\rho(R)}. \quad (28)$$

Fig. 14 shows the evolution of h for run A1 with time. The initial thick protostellar disk flattens to solar nebular disk with a disk height of a few tens of AU.

At the time when the protostellar disk first forms, it rotates close to a solid body with a angular velocity of $\Omega \sim 10^{-11} \text{ rad s}^{-1}$ whereas the outer envelope follows a rotation law according to its density distribution, i.e. $\Omega \propto r^{-1}$. Fig. 15 shows the evolution of the angular velocity for run A1: while the disk is slowly accreting gas to a core density of $\rho \sim 10^{-11} \text{ g cm}^{-3}$ its core spins up to $\Omega \sim 10^{-9} \text{ rad s}^{-1}$. These numbers show that the core region is rotationally supported against gravitational collapse, i.e. $\Omega \sim \sqrt{4\pi G \rho/3}$.

We show the mass accretion rate of the disk, \dot{M} , in Fig. 16 (run A1) and Fig. 17 (run B68). This quantity is defined by the standard vertically averaged continuity equation:

$$\frac{dM}{dt} = -2\pi v_r R \Sigma, \quad (29)$$

where v_r is the radial velocity in the disk. In the case of run A1 after the protostellar disk forms the mass accretion at the outer edge

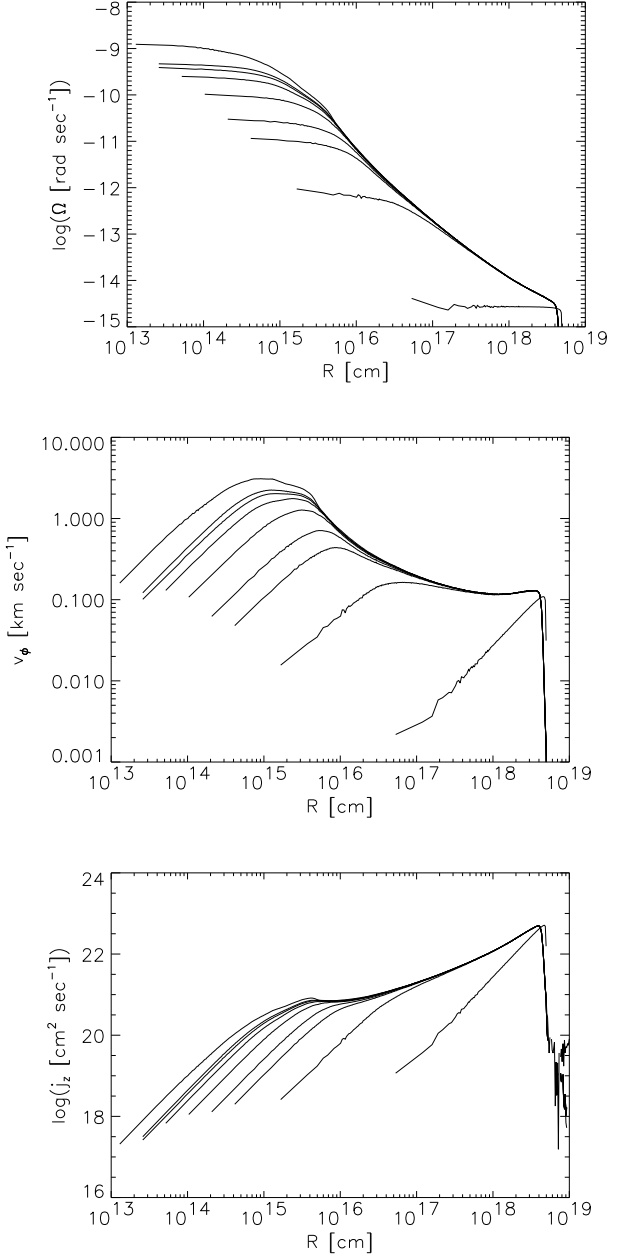


Figure 15. Radial profiles of the angular velocity Ω , the toroidal velocity v_ϕ , and the specific angular momentum j_z at different times. The shown profiles correspond to the density shown in Fig. 14 (run A1).

of the disk is $\sim 5 \times 10^{-4} M_\odot/\text{year}$ and increases slightly with time to $\sim 10^{-3} M_\odot/\text{year}$ while the disk radius decreases. For run B68 the mass accretion is highest at the ring's outer radius and reaches a maximal value of $\sim 3 \times 10^{-4} M_\odot/\text{year}$ there. Most of the infalling material is deposited at this outer rim of the disk and the mass accretion decreases towards the disk center as $\dot{M} \propto r$. The infalling gas outside of the disk reaches a constant terminal velocity of the order of the sound speed (cf. the radial velocity plot of Fig. 12) which results in a constant mass accretion in time in this outer region. In the second panel of Fig. 16 we compile the evolution of the total mass in the disk, $M_{\text{disk}}(R) = 2\pi \int dR R \Sigma$, for run A1 which reaches a few solar masses.

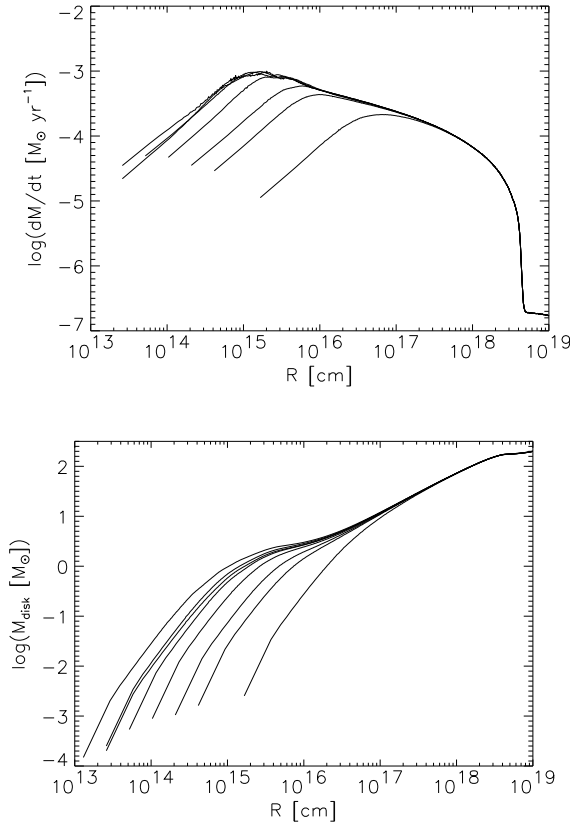


Figure 16. Radial profiles of the mass accretion \dot{M} and the cumulative disk mass M_{disk} at different times. The shown profiles correspond to the density shown in Fig. 11 (run A1).

5 DISK EVOLUTION: BARS, RINGS, AND FRAGMENTATION

Although we started all runs with a 10% $m = 2$ density perturbation, we did not observe any signs of fragmentation or non-central collapse in the isothermal regime. This is due to low mass (compared to the Jeans mass) in the collapsing core region (cf. Sec. 3.2). The first features which appear are a bar-type or ring-type structure. They are first evident after that stage of disk formation during which the non-isothermal core slowly accretes the surrounding gas.

It is known that thin disks are unstable to fragmentation if its Toomre Q -parameter (Toomre 1964)

$$Q = \frac{c \kappa}{\pi G \Sigma}, \quad (30)$$

becomes smaller than unity, where κ is the epicyclic frequency:

$$\kappa = \left(4\Omega^2 + R \frac{d\Omega^2}{dR} \right)^{1/2}. \quad (31)$$

The first unstable modes which are expected to grow and possibly persist for some dynamical times are the $m = 0$ ring-mode and $m = 2$ bar-mode. We find that a ring-type structure develops in the case with $t_{\text{ff}} \Omega = 0.2$ (runs A1 and B68) with a dimensionless radius of $\xi_{\text{ring}} \sim 6 \times 10^{-3}$. For run A2 this corresponds to a physical radius of ~ 300 AU and for run B68 to ~ 18 AU. In both cases the ring-structure persists only a few dynamical times and either fragments into a binary system (run A2) or collapses to a bar (run B68). In the case with $t_{\text{ff}} \Omega = 0.1$ (run A1) and $t_{\text{ff}} \Omega = 0.3$ (run

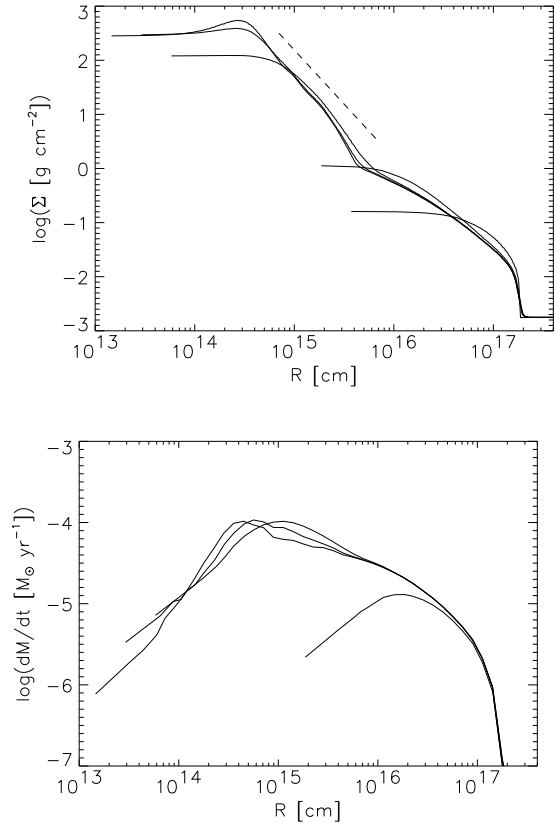


Figure 17. Similar figures than Fig. 16 and Fig. 14 for run B68. The ring structure is clearly visible in the surface density at late stages. The dotted line shows a R^{-2} profile.

A3) no such ring structures develop in the simulations. Instead a bar-like structure with spiral arms forms without a intermediate formation of a ring structure. A ring structure in the Coalsack Globule 2 was recently discovered by Lada et al. (2004). Our simulations may pertain to this system; in particular, since this cloud can be well described with a sub-critical Bonnor-Ebert profile.

We show 2D images of the density, temperature, and Q -parameter from the runs A_n and B68 at different times in Figs. 18 – 29. The bar that forms in the slow rotating run A1 shows no signs of fragmentation although the Q -parameter drops below unity when the bar density is very high, $> 10^{-8} \text{ g cm}^{-3}$. Slight instabilities in this high density and temperature (600 – 800 K) regime cannot grow quickly enough to lead to fragmentation as the inefficient cooling prevents a fast collapse of overdensities. In the case of faster rotation (run A2), instabilities form earlier resulting in a smaller Q -value than in run A1. These instabilities are large enough to lead to the fragmentation of the ring-type structure. In this situation, we observe the break-up into two fragments where each of them has a disk with spiral structure. These disks are surrounded with a circumstellar disk, and are connected by a tidal stream. The separation between the members of this binary system is ~ 260 AU which is roughly twice the size of the spiral structures itself. Each of these protostellar systems has a total mass of $\sim 1.3 M_{\odot}$. Run A3 with $t_{\text{ff}} \Omega = 0.3$ (Figs. 24 – 26) does not form a ring structure but collapses to a very twisted spiral arms and shows no sign of fragmentation. The simulation of Barnard 68 (run B68, Figs. 27 – 29) with $t_{\text{ff}} \Omega = 0.2$ results in a shortly lived ring structure which

collapses to a bar. This bar has a size of ~ 130 AU and a total mass of $\sim 0.1 M_\odot$.

The double-shock structure of these disks is easily seen in the density plots, as well as the temperature structure, and velocity fields in the x-z plane cuts.

The complex temperature structure due to cooling and the resulting pressure response in the non-isothermal regime prevents a simple analysis to decide which kind of structure one can expect from a rotating collapsing cloud. From our simulations we conclude that during the formation of the pre-stellar disk a ring structure appears at a radius of

$$\xi = \xi_{\text{ring}} = \xi_{\text{ring}}(t_{\text{ff}} \Omega) \quad , \quad (32)$$

whenever the cloud rotates fast enough. In order to decide whether such possibly formed ring will fragment into several pieces, one has to compare this radius with the size of the non-isothermal core where the enhanced thermal pressure stabilizes the core region against fragmentation. In section 3.1 we showed that the core radius of a collapsing Bonnor-Ebert-Sphere is (almost) independent of the initial cloud parameters and only determined by the density where $t_{\text{ff}} \sim t_{\text{cool}}$ (cf. Eq. 21). For a ring to fragment its size must not be much smaller than this warm core size which gives the condition

$$\xi_{\text{ring}} \sim \left(\frac{\rho_0}{\rho_{\text{core}}} \right)^{1/2} (\xi_c \phi'_c)^{1/2} \quad . \quad (33)$$

We find that ring structures which do not obey the condition (33) collapse to a single bar rather than fragmenting into two or more pieces. Figs. 27 to 28 show the time evolution of the density and temperature of the simulation B68 where a firstly formed ring condense to a bar. Note also that the core region rotates with $\Omega(r) \approx \text{const.}$ whereas the disk rotates differentially outside the core region (cf. Fig. 15) where shearing effects enhance instabilities. Another mechanism which facilitates the fragmentation of a ring structure is the appearance of a shock at the core edge. A ring structure of similar size as the core can accrete more material than smaller rings increasing the possibility of fragmentation.

In the case where $t_{\text{ff}} \Omega = 0.1$ (run A1), we find that a 2-armed spiral structure develops when $\rho_{\text{core}} \sim 10^{-11} \text{ g cm}^{-3}$ and $T \sim 200 \text{ K}$. If the initial sphere rotates with $t_{\text{ff}} \Omega = 0.2$ (run A2) a ring structure forms earlier when the density and temperature are respectively $\sim 10^{-14} \text{ g cm}^{-3}$ and $\sim 85 \text{ K}$. This confirms the general picture that slowly rotating clouds collapse to bars and thin filaments whereas faster rotating objects form a ring-type structure. Recent numerical investigation of rotating Bonnor-Ebert-Spheres by Matsumoto & Hanawa (2003) showed that spheres with $t_{\text{ff}} \Omega \approx 0.2$ collapse to a ring which fragments into several pieces.

The theory of bars in disk-like structures (see Binney & Tremaine 1987) predicts that the bar velocity Ω_b must be larger than the so called pattern velocity:

$$\Omega_p \equiv \Omega - \frac{1}{2} \kappa \quad (34)$$

of the disk. We show the evolution of the pattern velocity as a function of disk radius in Fig. 30. As the bar size, R_b is limited within the corotation radius R_{co} , where the corotation radius is given by $\Omega(R_{\text{co}}) = \Omega_b$, and the disk velocity falls off at the outer core the bar velocity is limited by:

$$\Omega_p < \Omega_b < \Omega \quad . \quad (35)$$

The disk velocity in the core region is roughly independent of the radius r which results in a small pattern velocity, e.g. $\Omega_p \ll \Omega$. Due to the different time scales of the core evolution $\sim t_{\text{ff}}$ and the

run	structure	$\Sigma \propto R^{-n}$	$\Omega_b [\text{rad s}^{-1}]$	$M_* [M_\odot]$
A1	bar	1.9	5×10^{-11}	2.5
A2	binary system	2.0	–	1.3 each
A3	bar & spirals	1.9	6×10^{-12}	2.2
B68	ring/bar	2.0	$\sim 10^{-10}$	0.1

Table 2. Summary of the simulation results. Where the disk profiles are measured in the non-isothermal regime, Ω_b is the bar velocity, and M_* is the central mass of the object(s).

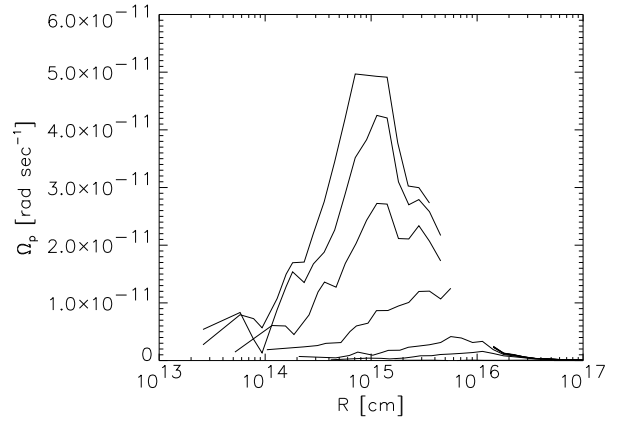


Figure 30. Evolution of the pattern velocity Ω_p as a function of radius R . The data are taken from run A1.

rotation period $\sim \Omega^{-1}$ where $t_{\text{ff}} \Omega \ll 1$ we were not able to follow a full rotation of the condensed bars. Nevertheless, we estimate the average bar speed for our different simulations (see table 2) as, few $\times 10^{-10}$ (run A1), few $\times 10^{-12}$ (run A3), and $\sim 10^{-10} \text{ rad s}^{-1}$ (run B68) which is in agreement with condition (35). Note that the run with the fastest initial rotation (run A3, $t_{\text{ff}} \Omega = 0.3$) results in the slowest bar velocity. This might be due to the fact the the bar of run A3 is much larger than the bar of run A1 ($t_{\text{ff}} \Omega = 0.1$) and its pronounced spiral arms released sufficient angular momentum to the surrounding disk.

Finally, we note that the column density profiles of the disks formed in our simulations are rather steep, obeying

$$\Sigma \propto R^{-1.95 \pm 0.05} \quad . \quad (36)$$

This is steeper than Hayashi models (Hayashi 1981) but in good agreement with disk models inferred from the measurement by Kuchner (2004) of planets in extrasolar systems, who found $\Sigma \propto R^{-2.0 \pm 0.5}$.

6 SUMMARY AND DISCUSSION

In this work we studied the collapse of rotating marginal stable Bonnor-Ebert-Spheres using 3D hydrodynamical simulations based on AMR technique. Compared to former numerical studies of collapsing molecular clouds, we included the effect of radiative cooling by molecular line emissions. This more realistic approach shows that the effective equation of state is a complex function of density and time during the collapsing phase and can not be approximated by a time independent EOS. Initially the gas cloud collapses

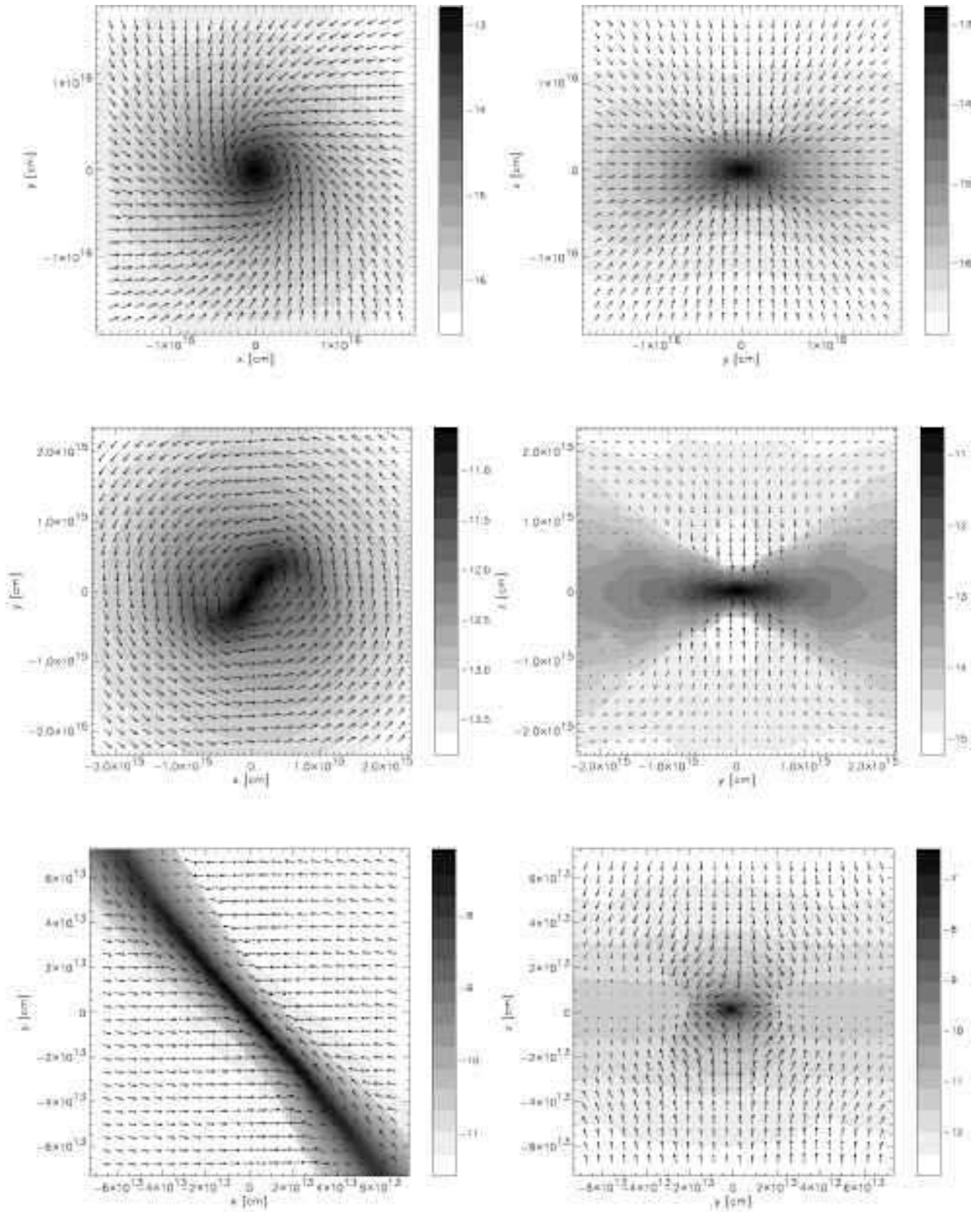


Figure 18. Shows 2D slices of the mass density (logarithmic scale in $[g\text{ cm}^{-3}]$) and velocity field at different times for run A1. After the protostellar disk forms a spiral feature builds up and collapses to a thin filament. The left panels and right panels show the evolution in the disk plane and perpendicular to the disk plane, respectively. Note that the highest resolution areas correspond (from top to bottom) to 256, 512, and 1024 pixels in each dimension.

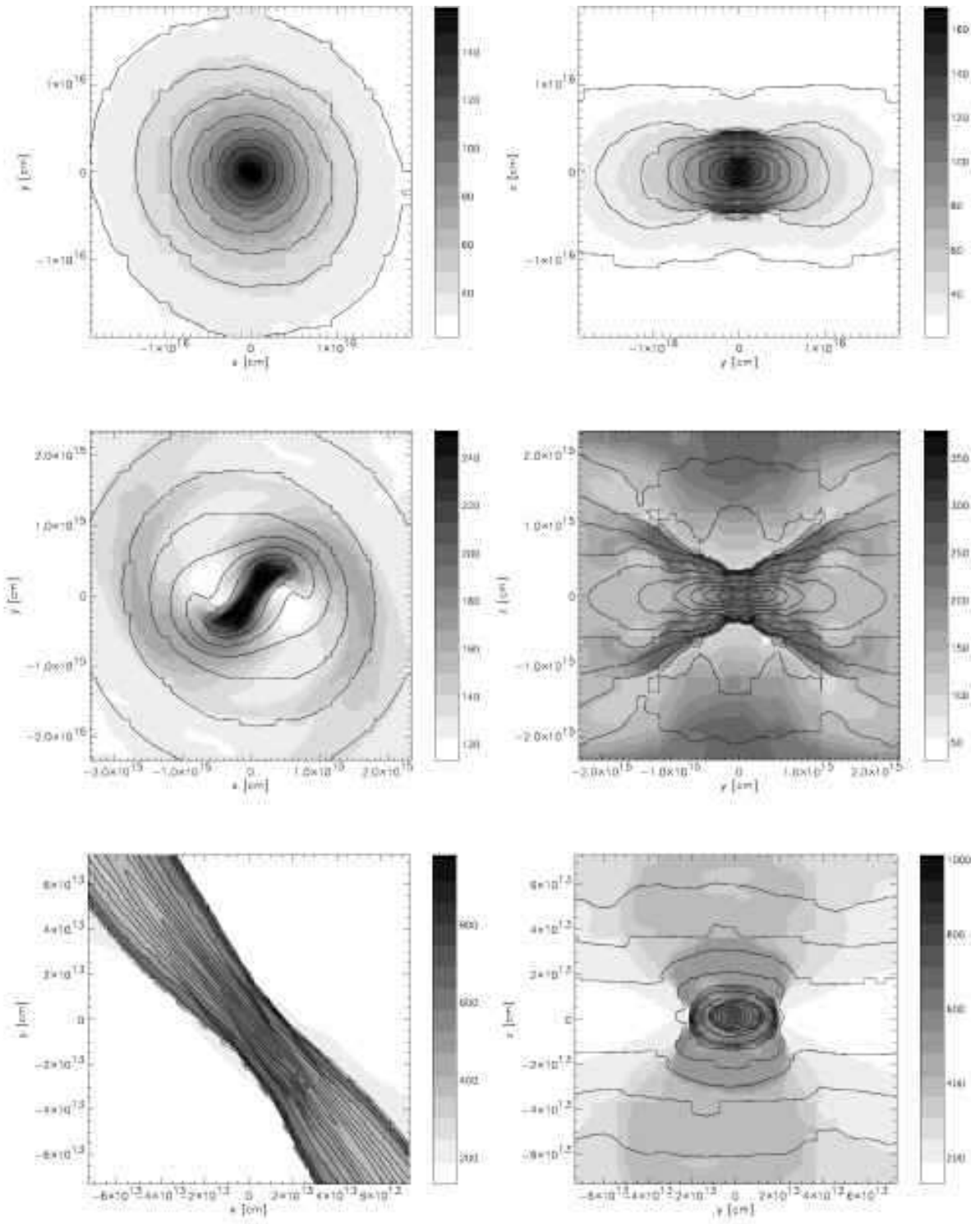


Figure 19. Evolution of the temperature field (gray scale in [K]) and density (contour lines). The panels correspond to these of Fig. 18 (run A1).

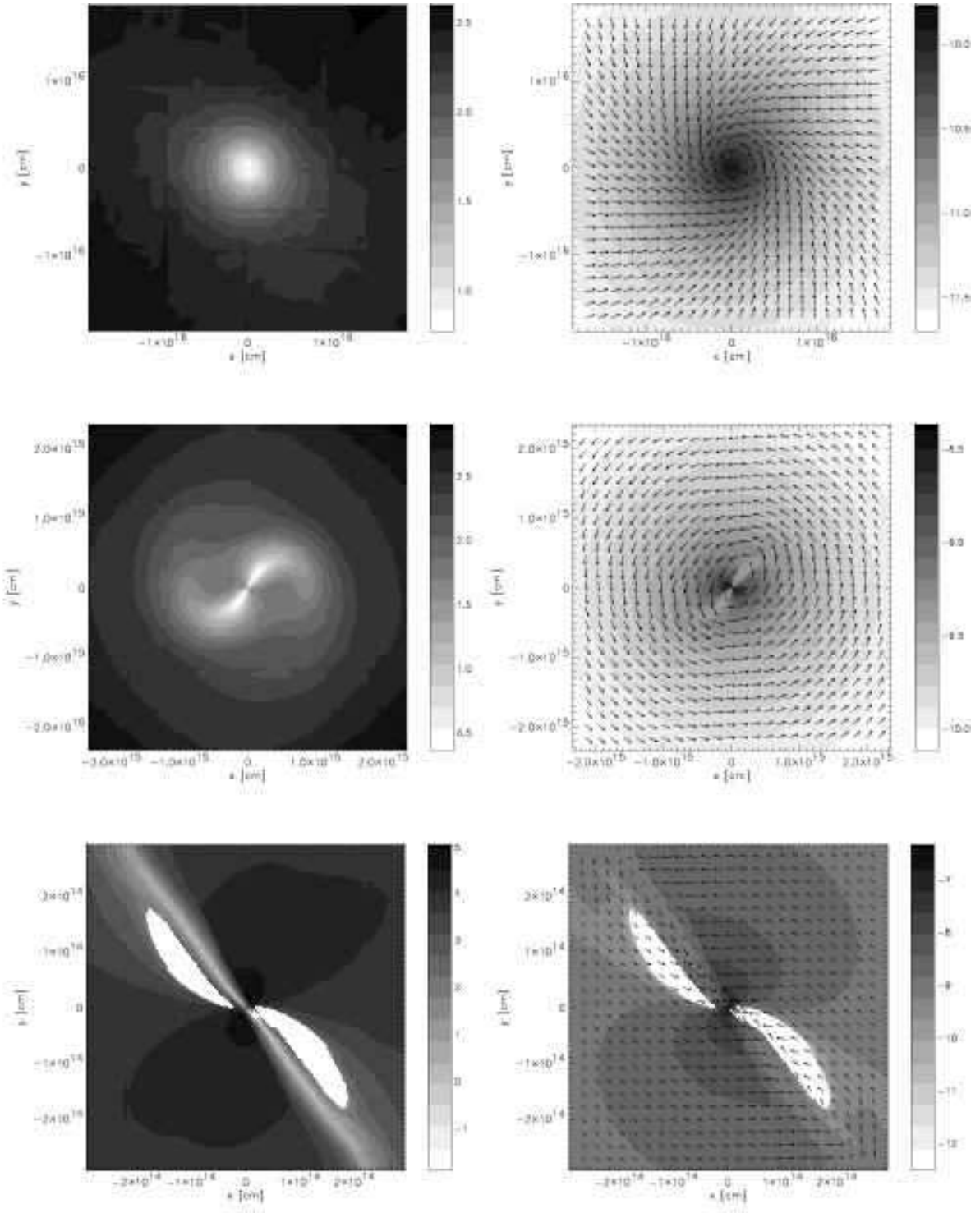


Figure 20. Shows the evolution of the Toomre Q -parameter (left panel, logarithmic scale) and the angular velocity Ω (right panel, logarithmic scale in rad s^{-1}). The panels correspond to these of Fig. 18 (run A1).

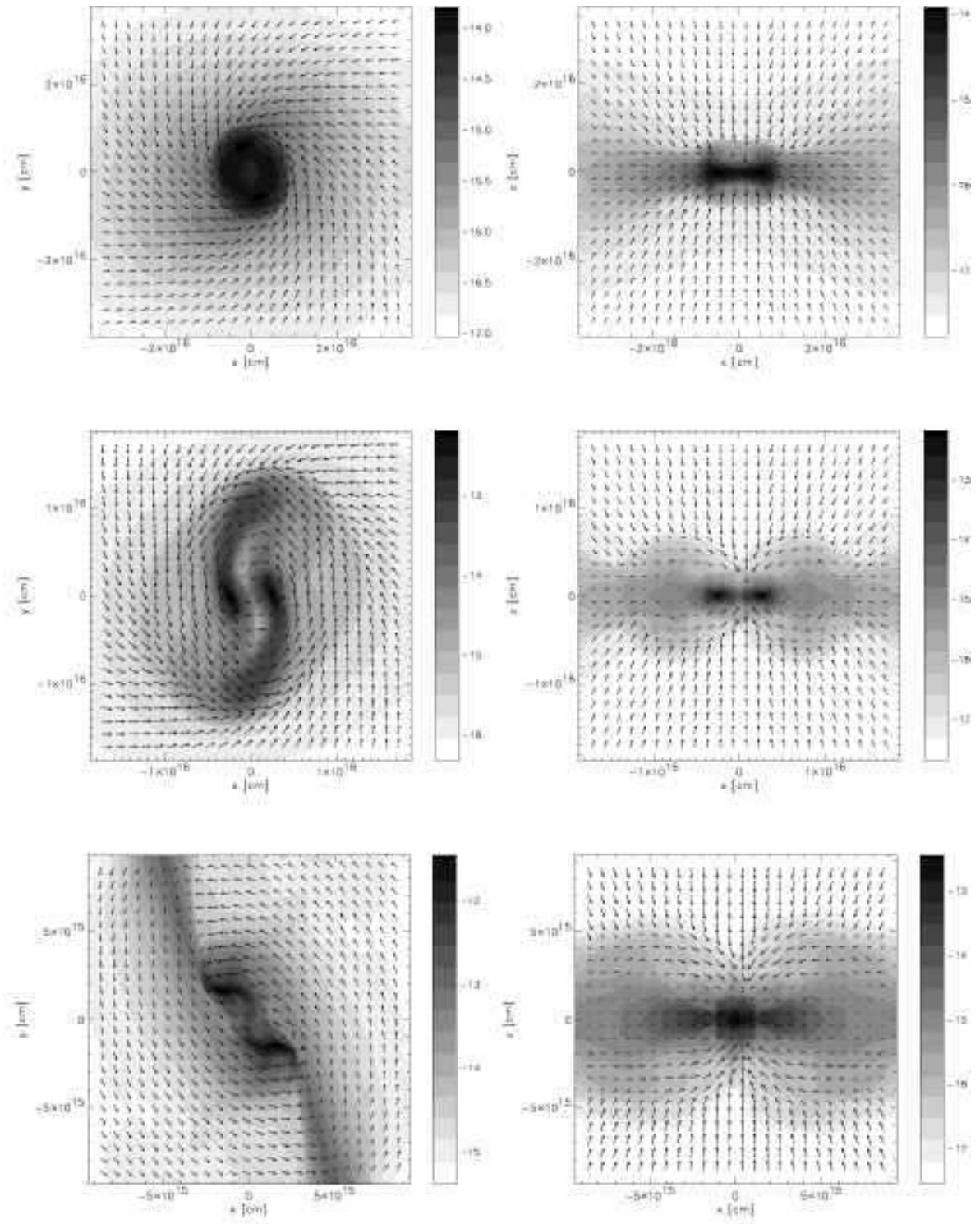


Figure 21. Shows 2D slices of the mass density (logarithmic scale in $[\text{g cm}^{-3}]$) and velocity field at different times for run A2.

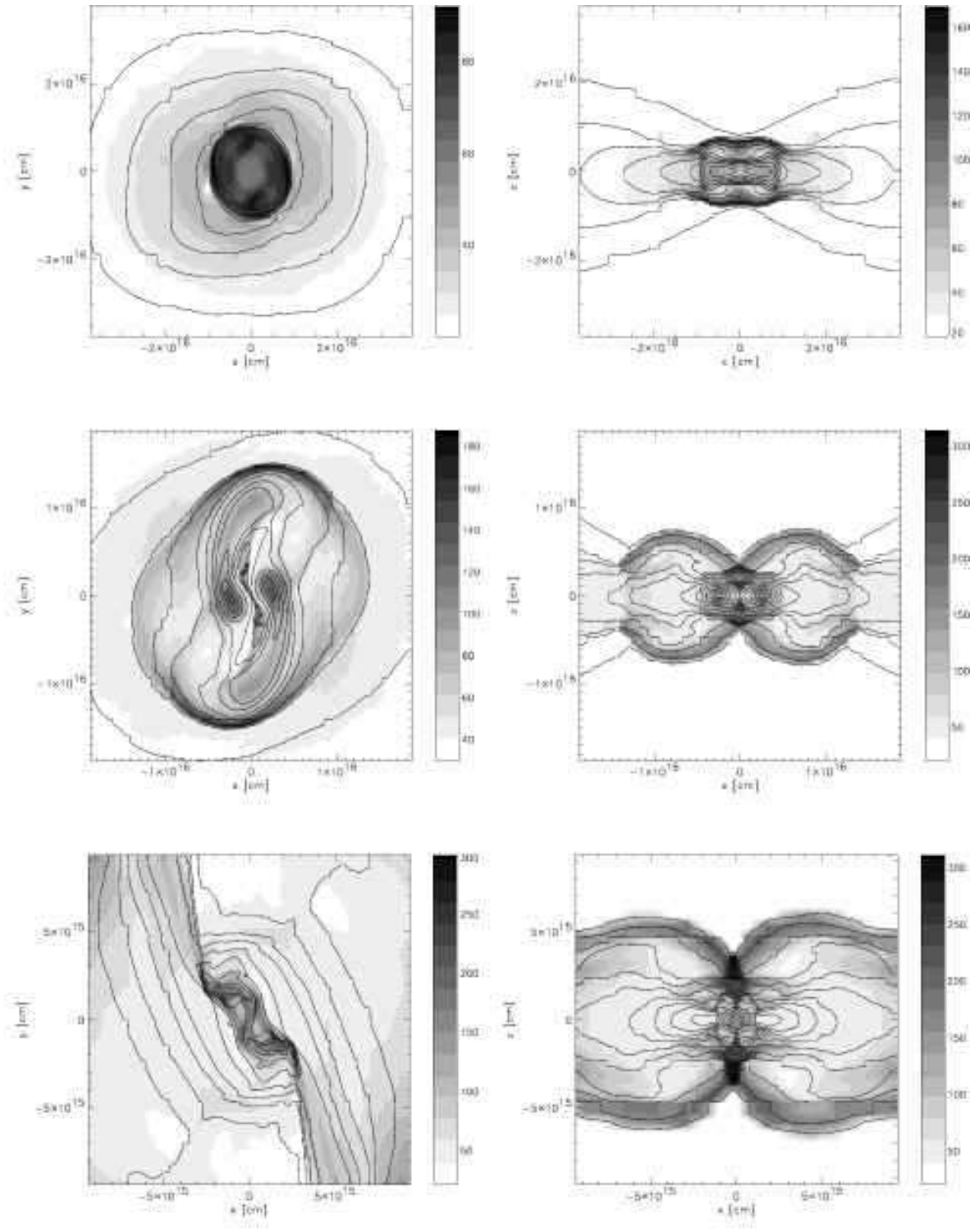


Figure 22. Evolution of the temperature field (gray scale in [K]) and density (contour lines). The panels correspond to these of Fig. 21 (run A2).

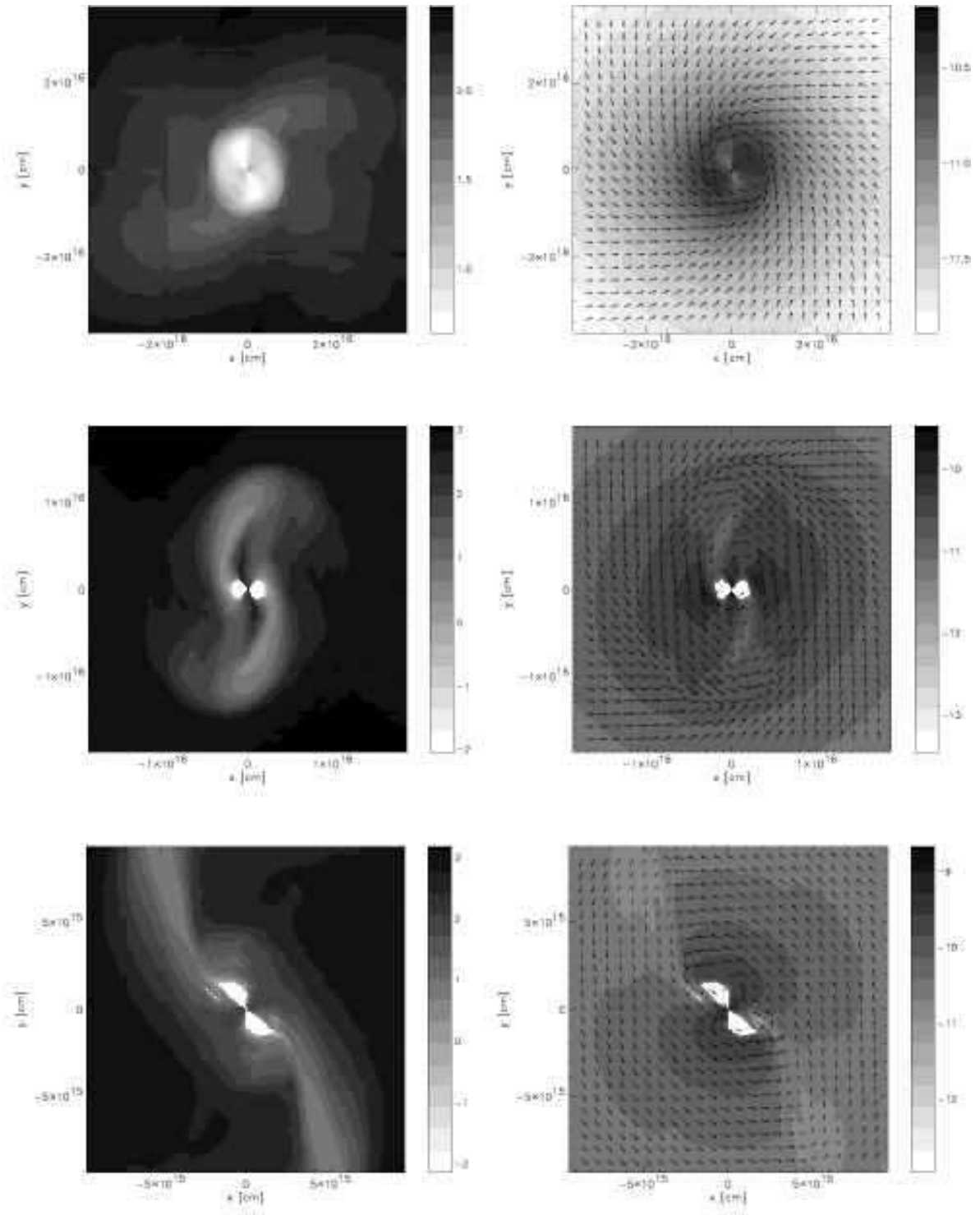


Figure 23. Shows the evolution of the Toomre Q -parameter (left panel, logarithmic scale) and the angular velocity Ω (right panel, logarithmic scale in rad s^{-1}). The panels correspond to these of Fig. 21 (run A2).

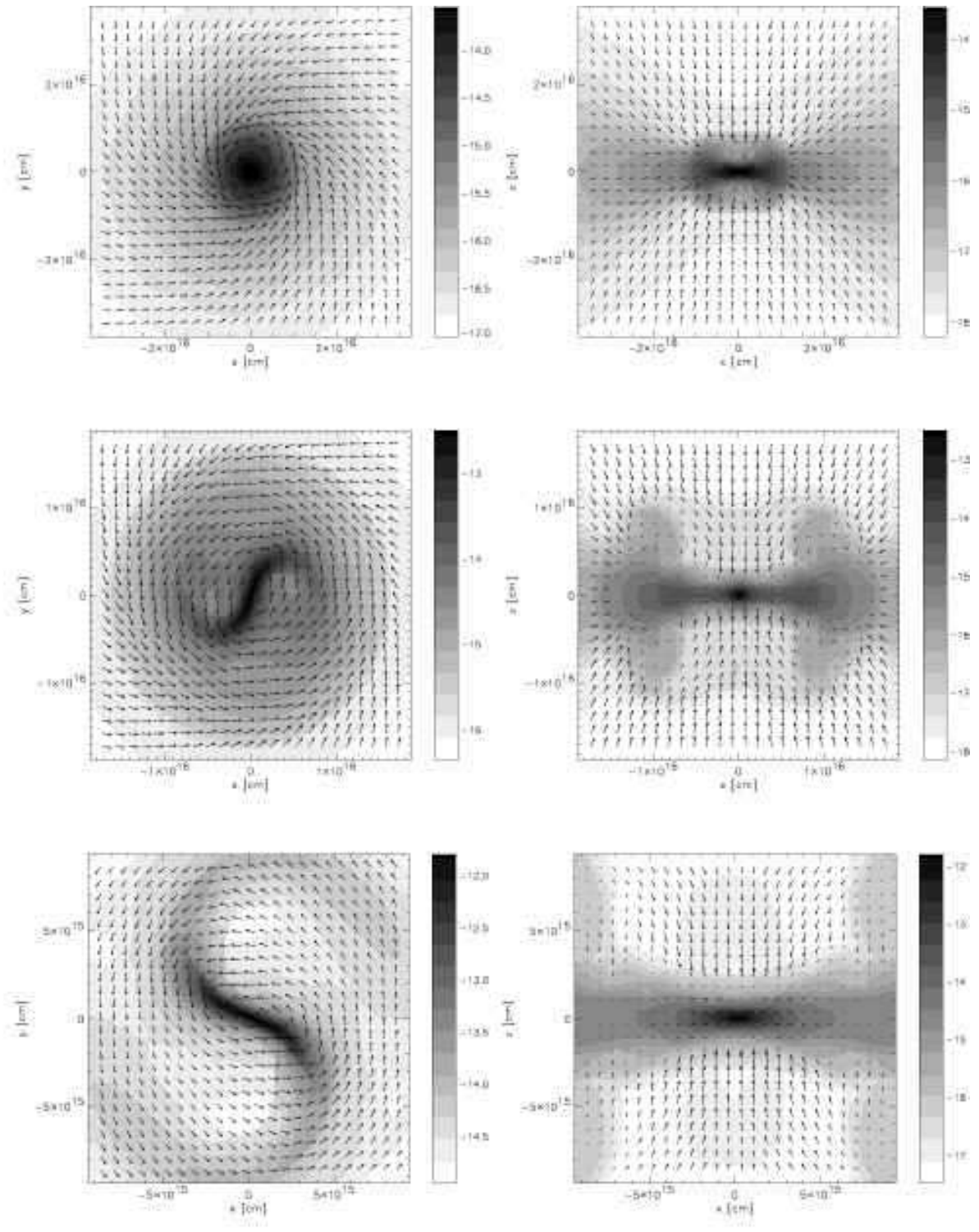


Figure 24. Shows 2D slices of the mass density (logarithmic scale in $[\text{g cm}^{-3}]$) and velocity field at different times for run A3.

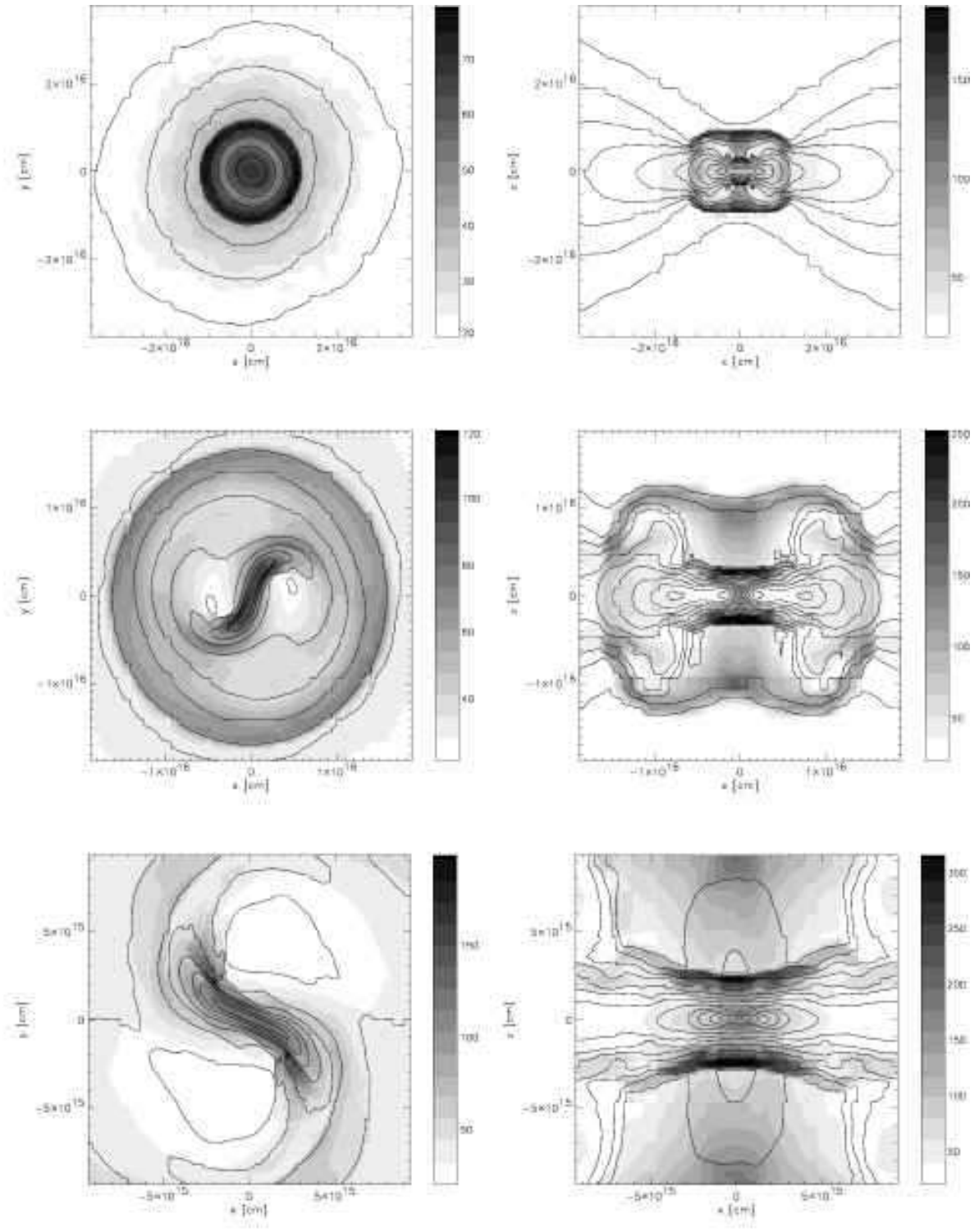


Figure 25. Evolution of the temperature field (gray scale in [K]) and density (contour lines). The panels correspond to these of Fig. 24 (run A3).

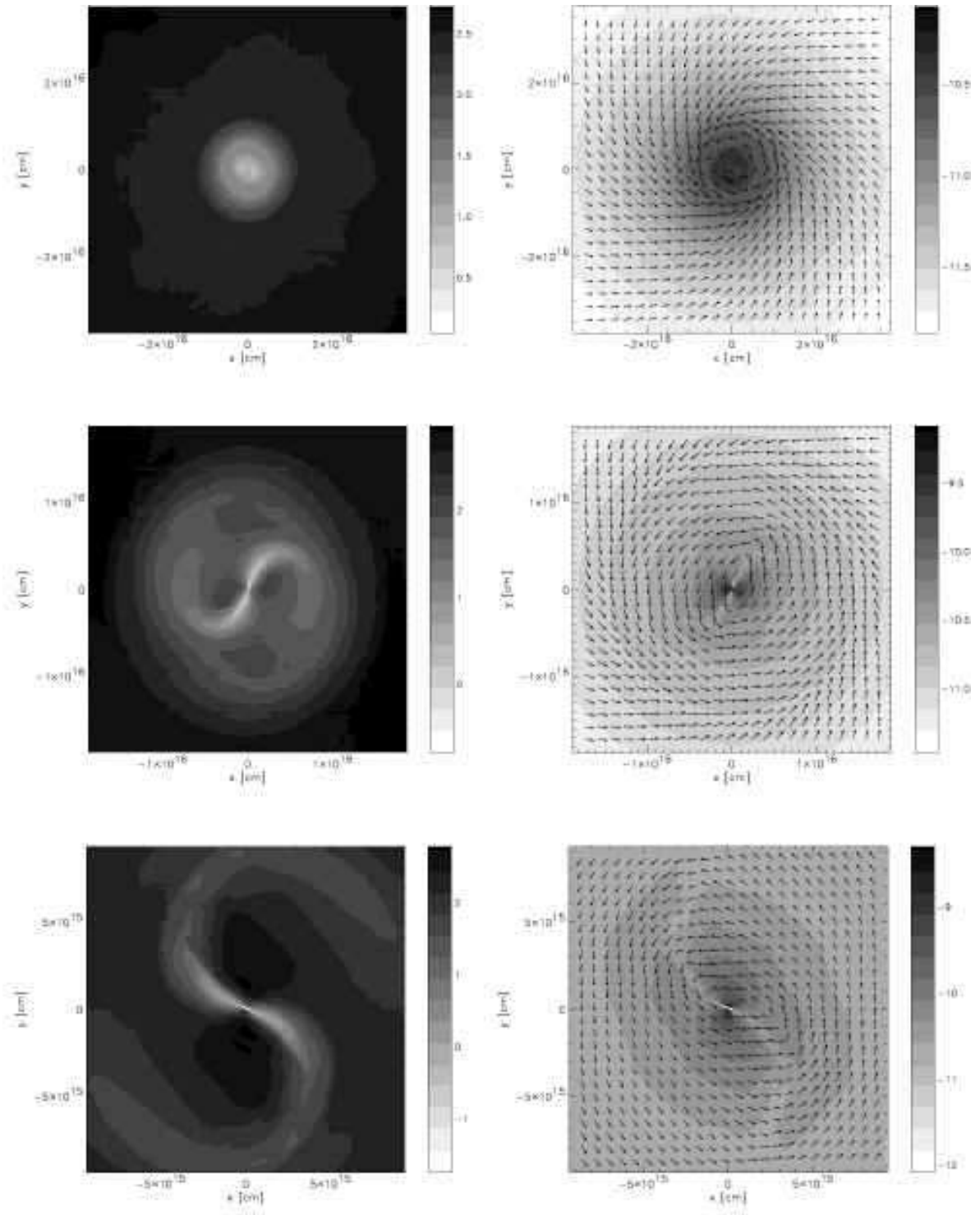


Figure 26. Shows the evolution of the Toomre Q -parameter (left panel, logarithmic scale) and the angular velocity Ω (right panel, logarithmic scale in rad s^{-1}). The panels correspond to these of Fig. 24 (run A3).

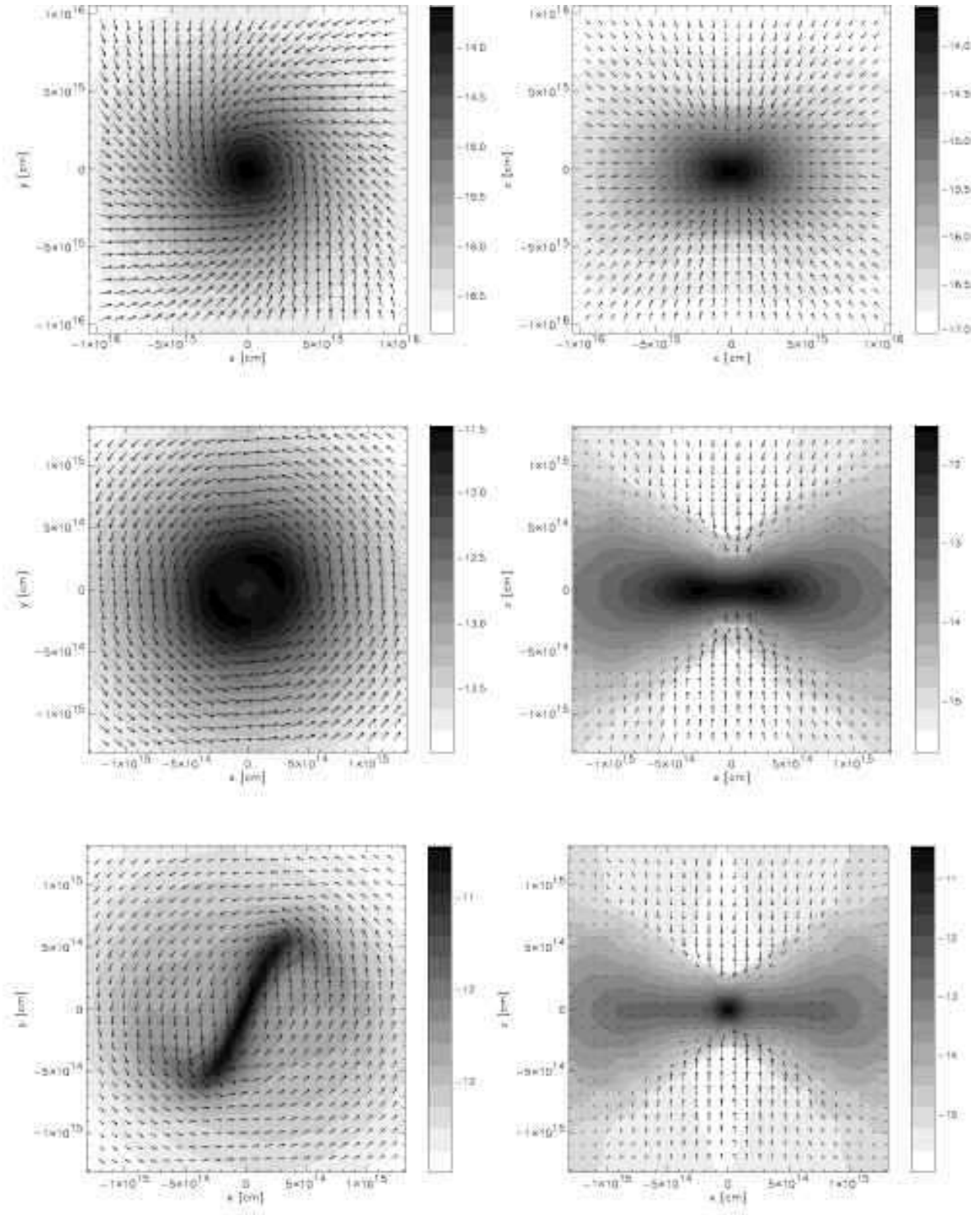


Figure 27. Shows 2D slices of the mass density (logarithmic scale in $[\text{g cm}^{-3}]$) and velocity field from the simulation B68 at different times: from top to bottom: $t = 5.35, 5.40, 5.41 t_{\text{ff}}$ corresponding $3.597, 3.628, 3.633 \times 10^5$ years.

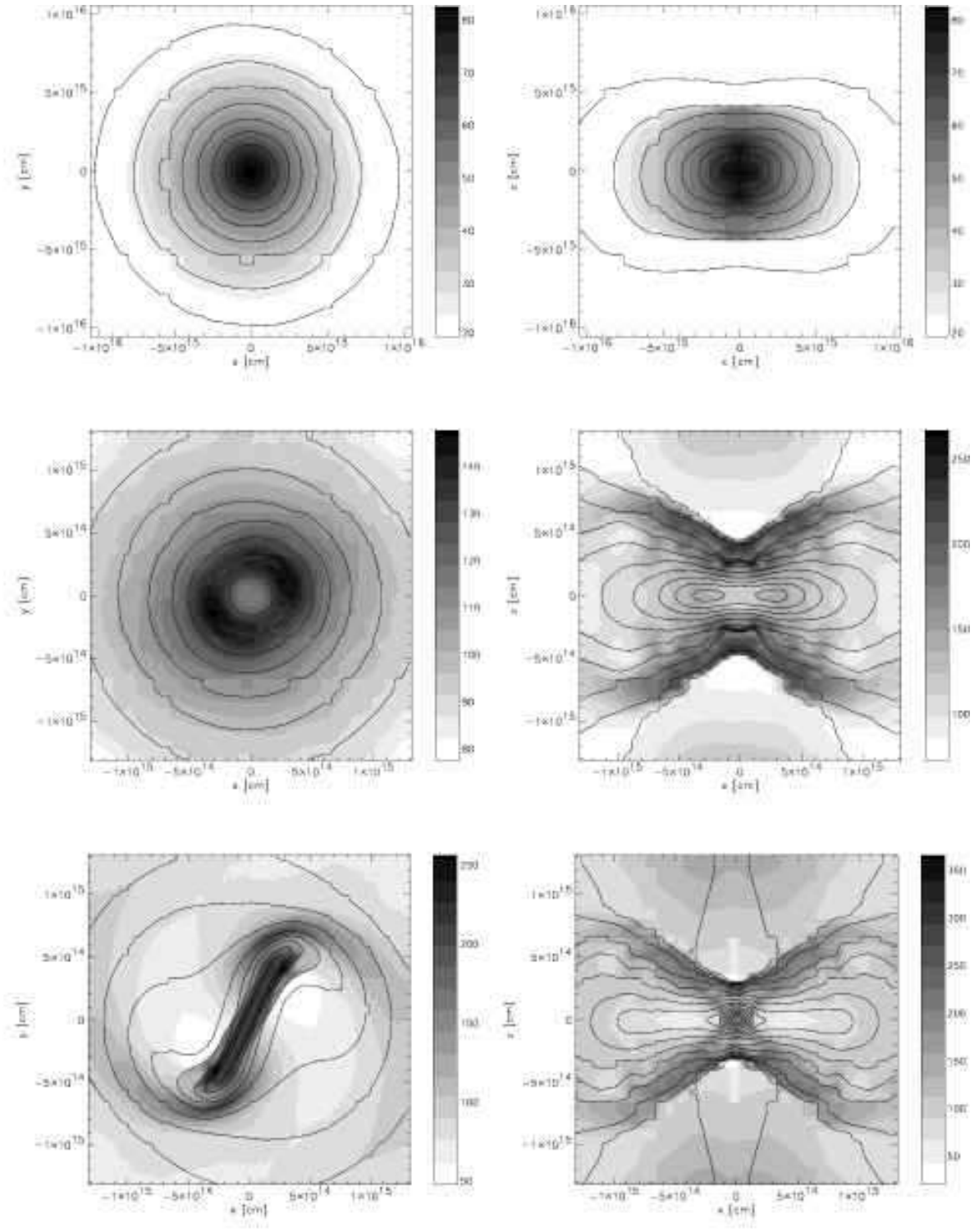


Figure 28. Evolution of the temperature field (gray scale in [K]) and density (contour lines). The panels correspond to these of Fig. 27 (run B68).

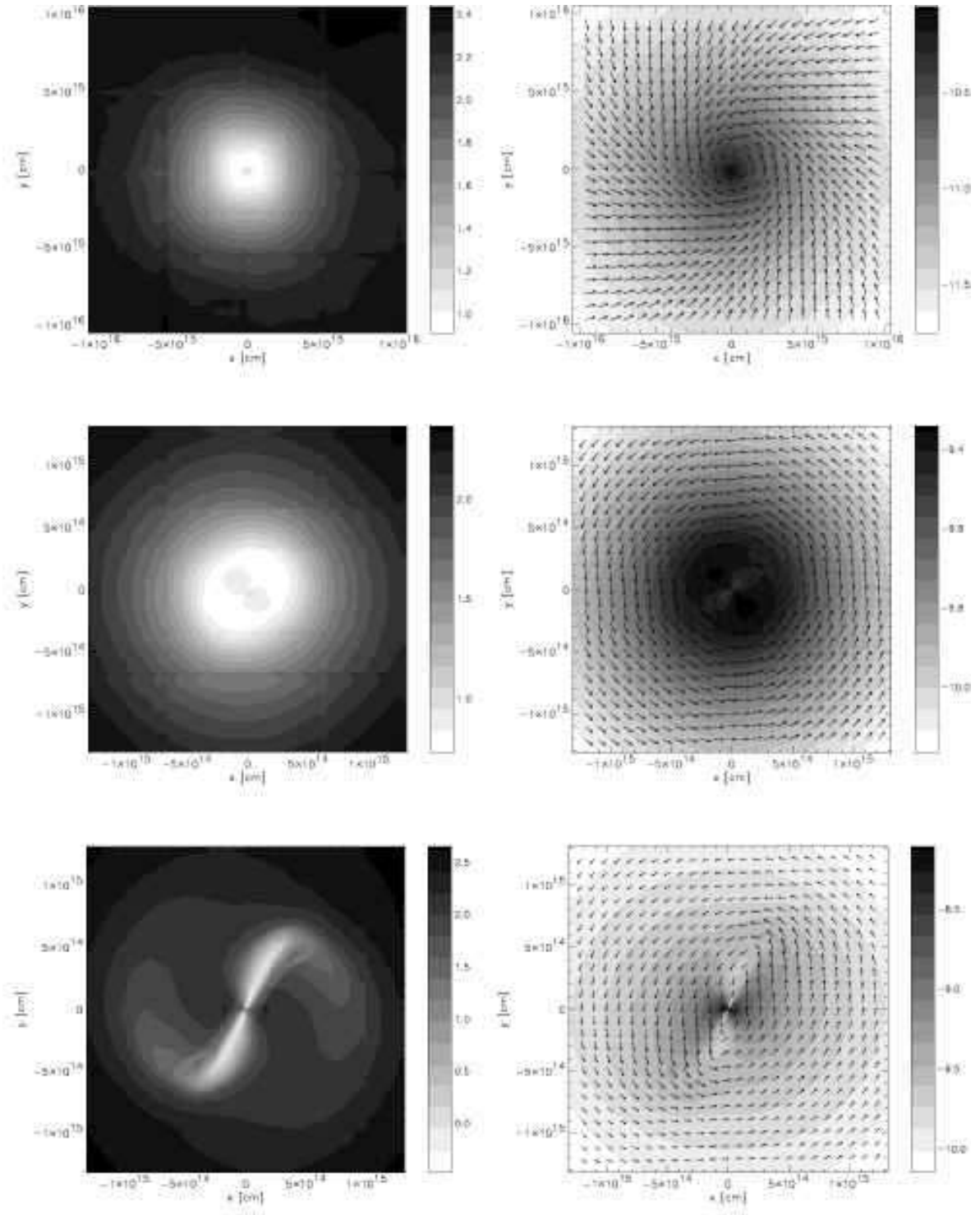


Figure 29. Shows the evolution of the Toomre Q -parameter (left panel, logarithmic scale) and the angular velocity Ω (right panel, logarithmic scale in $[\text{rad s}^{-1}]$). The panels correspond to these of Fig. 27 (run B68).

isothermally on a free fall time until the core density reaches the critical point where cooling becomes less efficient (i.e. $t_{\text{cool}} > t_{\text{ff}}$) at $n \sim 10^{7.5} \text{ cm}^{-3}$. During this isothermal phase the cloud collapses from outside-in where the density profile approaches to a (steadily increasing) flat core region with a r^{-2} envelope. The infall velocity peaks at the edge of the core where it reaches $\mathcal{M} \sim 3$ and drops to zero at the center of the gas cloud. Subsequently the temperature in core region starts to rise and an increasing pressure support stabilizes the gas clump preventing immediate fragmentation. As cold gas from the envelope falls onto the warm core region shock fronts build up, separating the cold envelope from the heated up core. All our simulations show a similar double shock structure: an early outer shock and a later inner shock. Both shock fronts move slowly toward the core center where the inner shock region sets the conditions for the first appearance of the protostellar disk. The appearance of these shocks determine also the accretion rate onto the core (resp. bar) as material outside the shock region is stalled at the shock boundaries. We find peak accretion rates for the low and high mass systems of $3 \times 10^{-4} M_{\odot}/\text{year}$ and $\sim 10^{-3} M_{\odot}/\text{year}$, respectively. In this work we did not keep track of the composition of the gas during the collapse of the molecular cloud, but its is known that the chemistry might be altered within the shock region (e.g. Jørgensen et al. 2004).

Depending on the initial rotation and density a ring mode or a bar develops in the disk plane. Only one of our four simulations result into the fragmentation of the protostellar disk. In this particular case, a ring structure developed first which then fragments into a binary system in which each system contains a bar structure. The preferred appearance of bars in our simulations supports theoretical predictions that the most likely growing instability mode in disks is the $m = 2$ bar mode.

Due to the limitations of our numerical scheme we are not able to follow the bar evolution for several rotation periods as the time scales of the bar rotation and core evolution diverge (i.e. $t_{\text{rot}} \gg t_{\text{ff}}$) shortly after the bar forms. Further fragmentation of the bars might happen during the phase of hydrogen dissociation ($T > 2000 \text{ K}$) where the effective equation of state drops below 4/3 or when tidal interactions of the spiral arms become stronger.

A comparison of our A2 simulations – which produces a distinct ring that fragments into a binary – with the recent observation of a massive disk in M 17 (Chini et al. 2004) is interesting. The observations reveal an inner torus (within a $100 M_{\odot}$ disk) whose radius is $\sim 3.8 \times 10^{16} \text{ cm}$. The radius of the dense initial ring that forms in our simulation A2 is of the same order ($\sim 10^{16} \text{ cm}$, see Fig. 21) which is in good agreement with these observations.

ACKNOWLEDGEMENT

The authors would like to thank Tom Abel and James Wadsley for useful and inspiring discussions. We are grateful to David Neufeld and his collaborators for providing us with their cooling data. Thanks also to the referee, Andreas Burkert, for useful comments. The FLASH code was in part developed by the DOE-supported Alliances Center for Astrophysical Thermonuclear Flashes (ASCI) at the University of Chicago. Our simulations were carried out on a 128 CPU AlphaServer SC, which is the McMaster University node of the SHARCNET HPC Consortium. R.B. is supported by the SHARCNET Postdoctoral Fellowship program, and R.E.P. is supported by the Natural Sciences and Engineering Research Council of Canada.

REFERENCES

- Alves J. F., Lada C. J., Lada E. A., 2001, *Nature*, 409, 159
 Bate M. R., Burkert A., 1997, *MNRAS*, 288, 1060
 Binney J., Tremaine S., 1987, *Galactic dynamics*. Princeton, NJ, Princeton University Press, 1987, 747 p.
 Bodenheimer P., Burkert A., Klein R. I., Boss A. P., 2000, *Protostars and Planets IV*, 675
 Bodenheimer P., Sweigart A., 1968, *ApJ*, 152, 515
 Bonnor W. B., 1956, *MNRAS*, 116, 351
 Boss A. P., 1993, *ApJ*, 410, 157
 Burkert A., Bodenheimer P., 1993, *MNRAS*, 264, 798
 Chandrasekhar S., 1967, *An introduction to the study of stellar structure*. New York: Dover, 1967
 Chini R., Hoffmeister V., Kimeswenger S., Nielbock M., Nürnberger D., Schmidtbreick L., Sterzik M., 2004, *Nature*, 429, 155
 Ebert R., 1955, *ZAp*, 37, 217
 Foster P. N., Chevalier R. A., 1993, *ApJ*, 416, 303
 Fryxell B., Olson K., Ricker P., Timmes F. X., Zingale M., Lamb D. Q., MacNeice P., Rosner R., Truran J. W., Tufo H., 2000, *ApJS*, 131, 273
 Harvey D. W. A., Wilner D. J., Lada C. J., Myers P. C., Alves J. F., Chen H., 2001, *ApJ*, 563, 903
 Hayashi C., 1981, *Progress of Theoretical Physics Supplement*, 70, 35
 Hayashi C., Nakano T., 1965, *Progr. Theoret. Phys.*, 34, 754
 Hunter C., 1977, *ApJ*, 218, 834
 Inutsuka S., Miyama S. M., 1992, *ApJ*, 388, 392
 Jørgensen J. K., Hogerheijde M. R., Blake G. A., van Dishoeck E. F., Mundy L. G., Schöier F. L., 2004, *A&A*, 415, 1021
 Kuchner M. J., 2004, astro-ph/0405536, to appear in *ApJ*
 Lada C. J., Bergin E. A., Alves J. F., Huard T. L., 2003, *ApJ*, 586, 286
 Lada C. J., Huard T. L., Crews L. J., Alves J. F., 2004, astro-ph/0404054, to appear in *ApJ*
 Larson R. B., 1969, *MNRAS*, 145, 271
 —, 2003, *Reports of Progress in Physics*, 66, 1651
 Matsumoto T., Hanawa T., 2003, *ApJ*, 595, 913
 McLaughlin D. E., Pudritz R. E., 1996, *ApJ*, 469, 194
 Neufeld D. A., Kaufman M. J., 1993, *ApJ*, 418, 263
 Neufeld D. A., Lepp S., Melnick G. J., 1995, *ApJS*, 100, 132
 Olson K. M., MacNeice P., Fryxell B., Ricker P., Timmes F. X., Zingale M., 1999, *Bulletin of the American Astronomical Society*, 31, 1430
 Penston M. V., 1969, *MNRAS*, 145, 457
 Racca G., Gómez M., Kenyon S. J., 2002, *AJ*, 124, 2178
 Shu F. H., 1977, *ApJ*, 214, 488
 Tilley D. A., Pudritz R. E., 2004, astro-ph/0404054, to appear in *MNRAS*
 Toomre A., 1964, *ApJ*, 139, 1217
 Truelove J. K., Klein R. I., McKee C. F., Holliman J. H., Howell L. H., Greenough J. A., 1997, *ApJ*, 489, L179+
 Truelove J. K., Klein R. I., McKee C. F., Holliman J. H., Howell L. H., Greenough J. A., Woods D. T., 1998, *ApJ*, 495, 821
 Yorke H. W., Bodenheimer P., Laughlin G., 1995, *ApJ*, 443, 199
 Yorke H. W., Sonnhalter C., 2002, *ApJ*, 569, 846